A critical evaluation of the ability of the Spinning Enhanced Visible and Infrared Imager (SEVIRI) thermal infrared red-green-blue rendering to identify dust events: theoretical analysis

A critical evaluation of the ability of the Spinning Enhanced Visible and Infrared Imager (SEVIRI) thermal infrared red-green-blue rendering to identify dust events: Theoretical analysis

Helen Brindley,[1] Peter Knippertz,[2] Claire Ryder,[3] and Ian Ashpole[4]

Received 14 December 2011; revised 20 February 2012; accepted 23 February 2012; published 3 April 2012.

[1] Using a combination of idealized radiative transfer simulations and a case study from the first field campaign of the Saharan Mineral Dust Experiment (SAMUM) in southern Morocco, this paper provides a systematic assessment of the limitations of the widely used Spinning Enhanced Visible and Infrared Imager (SEVIRI) red-green-blue (RGB) thermal infrared dust product. Both analyses indicate that the ability of the product to identify dust, via its characteristic pink coloring, is strongly dependent on the column water vapor, the lower tropospheric lapse rate, and dust altitude. In particular, when column water vapor exceeds ~20–25 mm, dust presence, even for visible optical depths of the order 0.8, is effectively masked. Variability in dust optical properties also has a marked impact on the imagery, primarily as a result of variability in dust composition. There is a moderate sensitivity to the satellite viewing geometry, particularly in moist conditions. The underlying surface can act to confound the signal seen through variations in spectral emissivity, which are predominantly manifested in the 8.7 μm SEVIRI channel. In addition, if a temperature inversion is present, typical of early morning conditions over the Sahara and Sahel, an increased dust loading can actually reduce the pink coloring of the RGB image compared to pristine conditions. Attempts to match specific SEVIRI observations to simulations using SAMUM measurements are challenging because of high uncertainties in surface skin temperature and emissivity. Recommendations concerning the use and interpretation of the SEVIRI RGB imagery are provided on the basis of these findings.

Citation: Brindley, H., P. Knippertz, C. Ryder, and I. Ashpole (2012), A critical evaluation of the ability of the Spinning Enhanced Visible and Infrared Imager (SEVIRI) thermal infrared red-green-blue rendering to identify dust events: Theoretical analysis, *J. Geophys. Res.*, *117*, D07201, doi:10.1029/2011JD017326.

1. Introduction

[2] Imagery derived from the Spinning Enhanced Visible and Infrared Imager (SEVIRI) onboard the Meteosat Second Generation series of geostationary satellites is routinely exploited for a wide variety of forecasting and hazard monitoring applications [e.g., *Martinez et al.*, 2009]. By selectively combining the information from different wavelength channels, red-green-blue (RGB) composite images can be produced, which offer the potential to identify specific features, while the high temporal resolution of SEVIRI allows these features to be tracked forward or backward in time. *Lensky and Rosenfeld* [2008] (hereafter LR08) describe several such channel combinations developed primarily for the analysis of rapid cloud, aerosol, and precipitation interactions. Among the various schemes is one designed to identify and monitor desert dust events using the information content within three thermal infrared (IR) channels (see Figure 13 for an example). Imagery produced using this rendering has been widely employed by the scientific community as a tool (1) to identify dust sources and activation [*Schepanski et al.*, 2007], (2) to assist with field campaign planning including aircraft in-flight routing, (3) to probe particular dust generation mechanisms and transport visually [e.g., *Marsham et al.*, 2008; *Knippertz*, 2008; *Schepanski et al.*, 2009; *Bou Karam et al.*, 2010; *Knippertz and Todd*, 2010], and (4) to qualitatively assess dust forecast model performance [e.g., *Johnson et al.*, 2011]. Since the SEVIRI field of view extends across approximately 70°N–70°S and 70°E–70°W, the instrument is ideally placed to monitor events originating from both African and Arabian dust sources. To date most studies using the imagery have focused on the Sahara and Sahel, although efforts have recently been made to assess its potential for identifying activity from southern African dust sources [*Vickery*, 2010].

[1]Space and Atmospheric Physics Group, Imperial College London, London, UK.
[2]School of Earth and Environment, University of Leeds, Leeds, UK.
[3]Department of Meteorology, University of Reading, Reading, UK.
[4]School of Geography and the Environment, University of Oxford, Oxford, UK.

0148-0227/12/2011JD017326

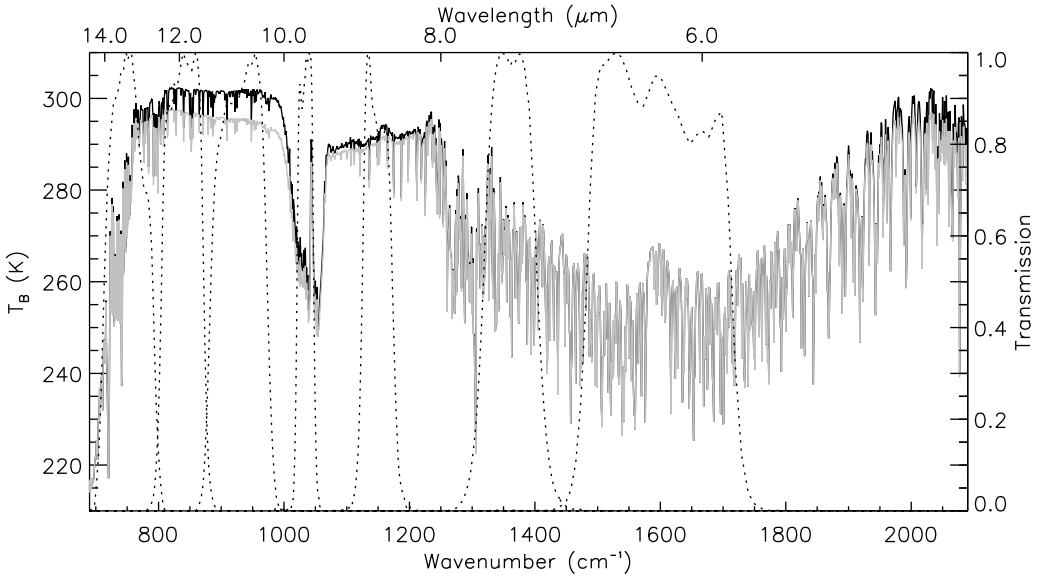

Figure 1. Characteristics of the seven mid-IR (4.5–14.5 μm) narrow-band channels of the Spinning Enhanced Visible and Infrared Imager (SEVIRI) on Meteosat-9 (dashed lines). Also shown are simulated T_B spectra representative of pristine (black) and dusty conditions (gray) over a barren desert surface using the mean June 10:30 UTC atmospheric profile observed at Niamey (Niger) during 2006 (see Table 2 for full details).

[3] Nevertheless, as recognized by many of the above authors, interpretation of the imagery is subjective, and the rendering may fail to produce an unambiguous dust signal under certain conditions. Particular candidates that may confound the identification of a dust signature include high levels of atmospheric water vapor, a strong near-surface temperature inversion, the height of the dust layer, the characteristics of the underlying surface, the dust mineralogical composition, and the size of the dust particles. For example, *Knippertz and Todd* [2010] show that large discrepancies can exist between regions visually identified as dusty using the LR08 rendering and elevated values of the aerosol index (AI) derived from the Ozone Monitoring Instrument (OMI), typically interpreted as indicative of dust presence [*Torres et al.*, 2007]. They suggest that this discrepancy is most likely due to high humidity in the specific regions analyzed. However, it should be noted that the OMI AI is also sensitive to other absorbing aerosols such as soot originating from biomass burning, which can strongly contribute to, or dominate the total aerosol loading in sub-Saharan Africa dependent on season. OMI AI also has a reduced sensitivity to low-altitude aerosol. Both of these factors may also contribute to the discrepancies seen.

[4] In this paper we seek to perform a more quantitative analysis of the ability of the SEVIRI dust RGB imagery to identify dust presence. This work is partly motivated by the findings of the previous studies discussed above, but also by ongoing projects such as the UK-led Fennec observational and modeling campaign, designed to better understand the complex dust-radiation-dynamical interactions within the Saharan Heat Low. As part of this project SEVIRI dust imagery is produced in near real time at Imperial College (see http://www.fennec.imperial.ac.uk) to aid campaign planning and for subsequent postcampaign analysis. Hence it is important to ascertain under what conditions the imagery is likely to be unable to identify dust presence. The organization of the paper is as follows: in section 2 we briefly recap the characteristics of SEVIRI and the methodology used to generate the dust images. Section 3 describes theoretical calculations performed in order to provide an insight into the sensitivity of the imagery to the various candidates identified above. In section 4 we focus on examples of specific dust events seen during the first field campaign of the Saharan Mineral Dust Experiment (SAMUM) during May–June 2006 [*Heintzenberg*, 2009] to assess whether the inferences gained from the theoretical analysis are consistent with observation. Finally, conclusions to be drawn from this work are presented in section 5.

2. SEVIRI Characteristics and Dust Imagery Production

[5] The spectral response functions of the seven mid-IR (4.5–14.5 μm) narrow-band channels of SEVIRI on Meteosat-9, the current operational satellite platform, are shown in Figure 1. Meteosat-9 is located at 0°E, 0°N, and each SEVIRI narrow-band channel has a spatial sampling rate of 3.0 km at the subsatellite point, with a temporal resolution of 15 min. Also shown in Figure 1 are simulated brightness temperature (T_B) spectra representative of pristine and dusty conditions over a barren desert surface for a specific atmospheric profile. More details concerning the simulations are provided in section 3, but comparing the spectral signature seen in the pristine-sky case to that seen when the dust layer is present illustrates the sensitivity of the SEVIRI channels to dust presence. The strongest signals are seen in the atmospheric window channels centered at 8.7, 10.8, and 12.0 μm. Atmospheric absorption due to water vapor, carbon dioxide, and ozone above the dust layer masks the dust signal in the remaining channels highlighted here.

Table 1. Gamma Correction and Scaling Range for Each Channel Appropriate for RGB Dust Imagery Rendering[a]

RGB Channel	Min_{ch} (K)	Max_{ch} (K)	Γ_{ch}
Red	−4.0	2.0	1.0
Green	0.0	15.0	2.5
Blue	261.0	289.0	1.0

[a]After *Lensky and Rosenfeld* [2008].

Given this sensitivity, the three window channels are combined to produce the standard dust imagery RGB rendering (LR08). One obtains the required intensity range in each channel, Int_{ch} using

$$Int_R = 255 \times \left[\frac{(T_{B120} - T_{B108}) - Min_R}{Max_R - Min_R}\right]^{\frac{1}{\Gamma_R}} \quad (1a)$$

$$Int_G = 255 \times \left[\frac{(T_{B108} - T_{B087}) - Min_G}{Max_G - Min_G}\right]^{\frac{1}{\Gamma_G}} \quad (1b)$$

$$Int_B = 255 \times \left[\frac{T_{B108} - Min_B}{Max_B - Min_B}\right]^{\frac{1}{\Gamma_B}} \quad (1c)$$

where $T_{B\lambda}$ is the brightness temperature in the relevant wavelength channel and Min_{ch}, Max_{ch}, and Γ_{ch} take the values given in Table 1. Values above 255 (below 0) are set to 255 (0). The channel brightness temperatures themselves are obtained from the measured counts in a two-step procedure. First the counts, C, are converted to channel radiance, L_{ch} (mW m^{-2} sr^{-1} $(cm^{-1})^{-1}$), using

$$L_{ch} = (Cg + os) \quad (2a)$$

where g and os are the appropriate channel gain and offset, respectively; then

$$T_{B\lambda} = \frac{c_2\nu}{\ln(1 + c_1\nu^3/L_{ch})} \quad (2b)$$

where ν is the channel wave number and c_1 and c_2 are the appropriate Planck radiation constants. This conversion is employed to ensure consistency with the manner in which the observations used here were originally calibrated.

[6] As noted by LR08 and apparent from Table 1 and Figure 1, the blue channel (equation (1c)) will tend to saturate (reach or exceed 255) over hot desert sands with minimal dust presence. The red and green channels will also have high intensities because T_{B108}-T_{B087} and T_{B120}-T_{B108} will tend to be near Max_R and Max_G, respectively, resulting in a whitish/pale blue signal. With an increasing airborne dust presence, the 10.8 μm channel tends to be suppressed faster than the 8.7 μm channel, reducing the green signal. Although the intensities in the blue and red channels are also affected, these changes happen at a slower rate such that the combined RGB signal turns pink.

3. Sensitivity Analysis of RGB Dust Signal

[7] Because of the number of parameters that could potentially influence the RGB dust signal it is difficult to generate an all-encompassing sensitivity analysis. The aim of this section is thus to generate a suitable subset of combined atmospheric, surface, and dust scenarios that can be considered broadly representative of generic conditions expected over the North African region. These will then be used to simulate the relevant SEVIRI channel T_Bs using spectrally resolved top of the atmosphere radiances computed with the MODTRAN4 radiative transfer code [*Anderson et al.*, 2000] with the relevant SEVIRI channel filter functions. The derived pseudo RGB dust imagery can then be visually and objectively assessed in terms of its ability to distinguish the presence of dust. Table 2 provides an overview of the full set of simulations performed and will be discussed parameter by parameter in section 3.1, while section 3.2 contains the actual simulation results. The main conclusions and the relevance for applications are summarized in section 3.3.

3.1. Radiative Transfer Input Fields

[8] The atmospheric temperature and water vapor profiles used here are derived from rawinsonde observations routinely collected by the Atmospheric Radiation Measurement Mobile Facility during its deployment at Niamey, Niger, through 2006 [*Miller and Slingo*, 2007]. Although it may seem counterintuitive to use data from only one location in a sensitivity analysis, Niamey is profoundly influenced by the West African monsoon and hence exhibits a strong seasonal variability in atmospheric conditions. Before monsoon onset the low-level atmospheric circulation is dominated by dry, northeasterly Harmattan flow resulting in high near-surface dustiness. The advance of the intertropical front from the southwest, typically reaching Niamey during early April, heralds monsoon onset, with enhanced cloud cover and water vapor burden, and reduced aerosol loading. In November the circulation tends to revert back to the pre-monsoon situation. Through 2006 atmospheric column water vapor (CWV) burdens varied from 3 mm prior to the wet season to greater than 60 mm during the late monsoon

Table 2. Summary of the Simulations Performed in Section 3[a]

Temperature and Dew Point Profile	Surface Emissivity	Viewing Zenith Angle	Dust Optical Properties	Dust Top Altitude	Dust Optical Depth
Niamey June and December means	Barren, 50%, and 100% fractional vegetation cover [after *Peres and DaCamara*, 2005]	0°, 30°, and 60°	Volz, Fouquart, WMO (*Haywood et al.* [2003, 2005] size distribution); WMO (largest mode removed); OPAC	1, 2, 3, and 4 km (base fixed at the surface)	0.0–1.0 in steps of 0.1, defined at 10 μm

[a]The control conditions for both June and December comprise the respective mean 10:30 UTC rawinsonde profile (Figure 2), dust optical properties after World Meteorological Organization (WMO) with the full Haywood size distribution, a barren surface, a dust top height of 3 km, and a viewing zenith angle of 30°. Each simulation covers the full optical depth range.

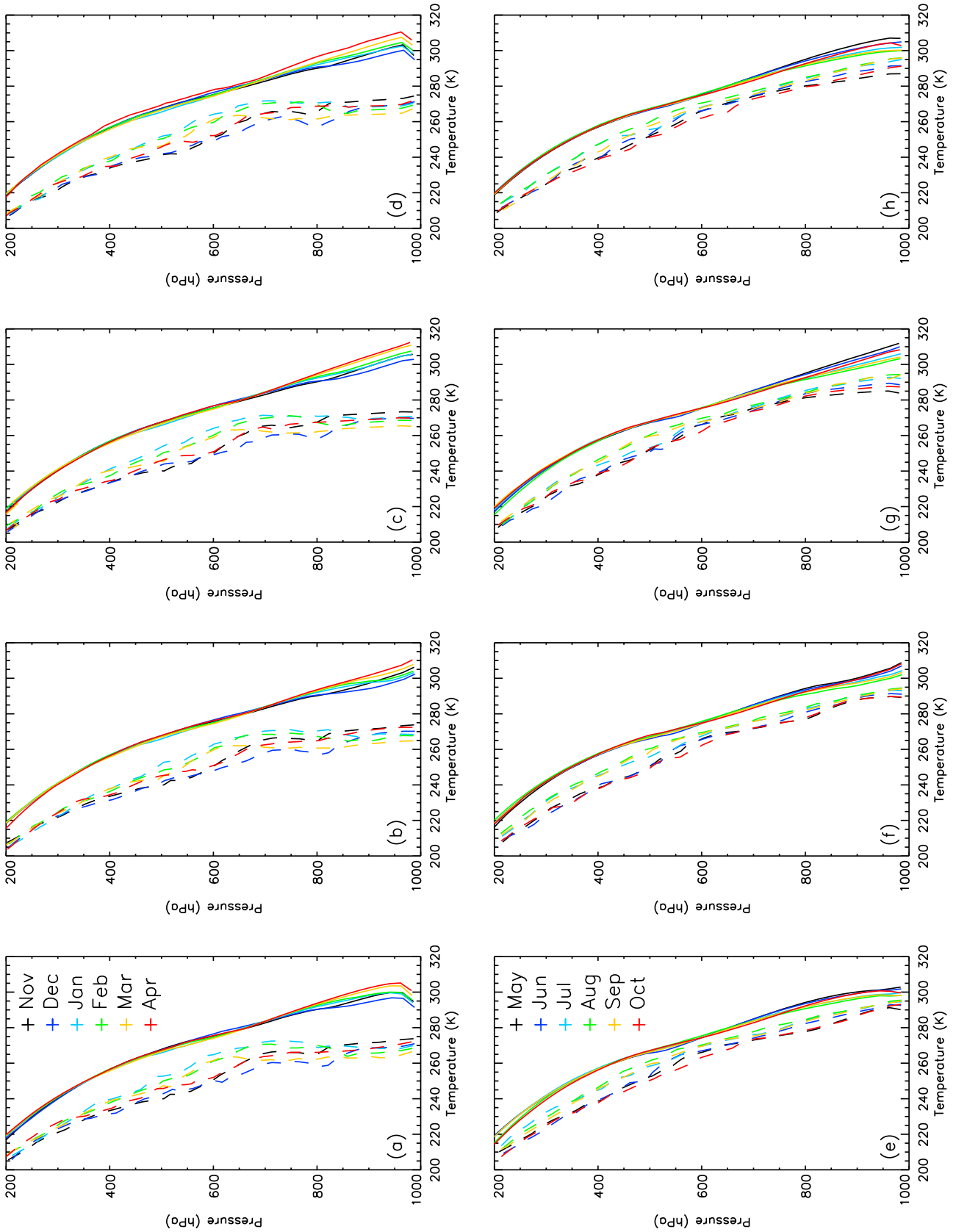
Nov
Dec
Jan
Feb
Mar
Apr
May
Jun
Jul
Aug
Sep
Oct
Pressure (hPa)
Temperature (K)
200
400
600
800
1000
200
220
240
260
280
300
320
(a)
(b)
(c)
(d)
(e)
(f)
(g)
(h)

Figure 2

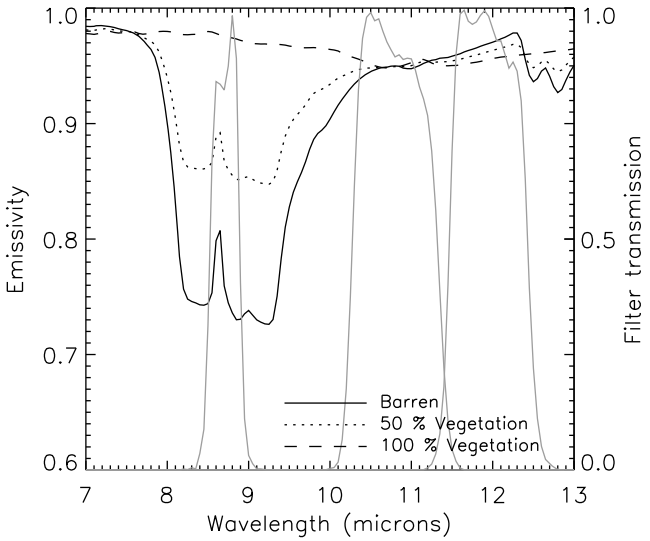

Figure 3. Spectral surface emissivities used for the simulations in section 3. The different lines show 0% (solid), 50% (dotted), and 100% (dashed) fractional vegetation cover. The 8.7, 10.8, and 12.0 μm SEVIRI filter functions are superposed.

[see *Slingo et al.*, 2008, Figure 8]. Figure 2 shows monthly mean dry-bulb and dew point temperature profiles constructed from the rawinsonde observations at 05:30, 10:30, 17:30, and 22:30 UTC. For each time slot the profiles have been crudely grouped into "nonmonsoon" (November–April) and "monsoon" (May–October) conditions. The tendency of those months falling in the latter category to be moister is clearly manifested in the reduced dew point departures seen at all times of day throughout the atmospheric column. In terms of atmospheric stability, as expected, the late morning and early afternoon observations in both categories demonstrate an enhanced near-surface temperature lapse rate compared with the early morning and late evening profiles. However, there is clearly greater diurnal variation in the nonmonsoon data, with the 05:30 and 22:30 UTC monthly mean profiles all showing near-surface temperature inversions (Figures 2a and 2d). This is a reflection of the effect of both reduced humidity and cloud cover, and associated enhanced nighttime surface radiative cooling to space over this period relative to the monsoon months. Given the obvious separation between the thermodynamic structure seen during the premonsoon and postmonsoon months and during the wet season, here we take the monthly mean December and June profiles as our baseline atmospheric states (first column in Table 2). Differences in the results obtained using each of these profiles will provide an insight into the effect of large perturbations to water vapor amount, while the diurnal information will help elucidate the role of the changes seen in near-surface temperature lapse rate.

[9] The impact of surface type is considered by performing simulations with varying surface emissivity characteristics. We use the approach described by *Peres and DaCamara* [2005] to generate the spectral surface emissivity for a standard barren surface, which is then systematically covered with vegetation. To reduce dimensionality in the final data set simulations are performed with 0%, 50%, and 100% fractional cover (second column in Table 2). Figure 3 indicates the spectral surface emissivity appropriate to each of these cases with the 8.7, 10.8, and 12.0 μm SEVIRI filter functions [*European Organisation for the Exploitation of Meteorological Satellites*, 2006] superposed. The strong dip between $\sim$8 and 9.5 μm for the barren case is due to silicate reststrahlen bands. Increasing the fractional vegetation cover masks this feature and reduces the spectral variability in the surface emissivity. The viewing zenith angle can influence the radiative signal through varying the path length through the atmosphere, which is simulated here for 0°, 30°, and 60° (third column in Table 2).

[10] Variability in the vertical location and the optical properties of any dust present has the potential to alter the radiative signal seen at the top of the atmosphere. *Sokolik and Toon* [1999] perform an extensive set of radiative transfer simulations to illustrate how changes to dust mineral composition and size distribution can have a profound effect on its spectral signature. *Turner* [2008] shows how ground-based measurements of spectrally resolved downwelling IR radiances can be used to discriminate between different mineral components, while several authors have investigated the potential of using IR satellite radiances from a variety of platforms to make inferences concerning dust optical depth and particle size or mineralogy [e.g., *DeSouza-Machado et al.*, 2006; *Li et al.*, 2007; *Klüser et al.*, 2011]. *Highwood et al.* [2003] use aircraft observations made during the SHADE campaign to help to constrain a set of radiative transfer simulations investigating the sensitivity of the measured upwelling IR radiances to dust properties and height. They found that the dust composition (expressed via dust refractive indices) and altitude had a more significant impact than realistic variations in the size distribution derived from AERONET measurements. However, more recent work [*McConnell et al.*, 2008, *Müller et al.*, 2010] has shown that differences between AERONET retrievals and aircraft size distributions derived from newer instrumentation can be significant for particle sizes >1 μm. These differences have a marked impact on dust optical properties at visible wavelengths, and would be expected to exert an even larger impact within the IR.

[11] Previous work by *Brindley and Russell* [2006] has shown that the different dust refractive indices considered by *Highwood et al.* [2003], from *Volz* [1973], *Fouquart et al.* [1987], and the World Meteorological Organization [*World Climate Program*, 1986], can produce markedly different signals in the red and green channels of the RGB dust product. Hence we make use of these data here (fourth

Figure 2. Vertical profiles of temperature and moisture used for the simulations in section 3. Monthly mean dry-bulb and dew point temperature profiles are constructed from rawinsonde observations at Niamey during 2006: (a, e) 05:30 UTC, (b, f) 10:30 UTC, (c, g) 17:30 UTC, and (d, h) 22:30 UTC. The profiles were resampled to a standard 50-level altitude grid running from the surface to 25 km and were grouped into nonmonsoon (November–April, Figures 2a–2d) and monsoon (May–October, Figures 2e–2h) conditions.

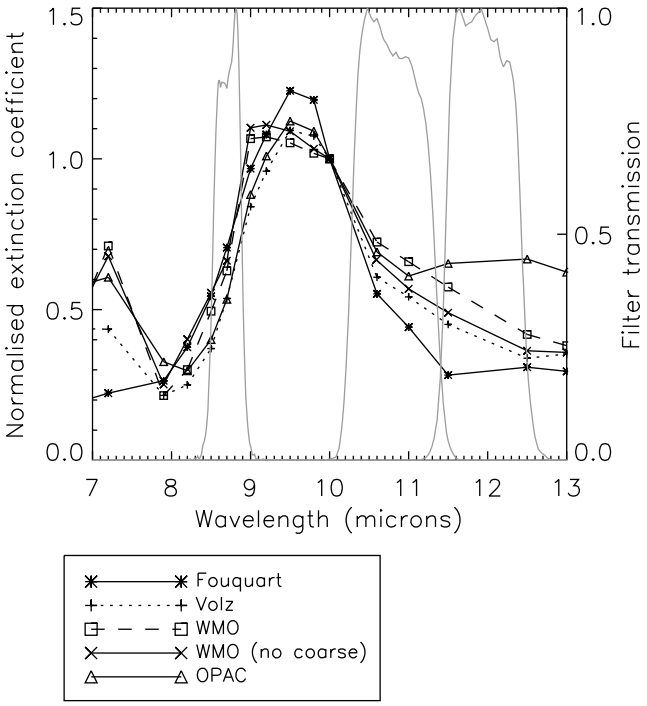

Figure 4. Dust optical properties used for the simulations in section 3. The extinction coefficient is normalized to 10 μm for five different dust representations (see section 3.1 for more details). The 8.7, 10.8, and 12.0 μm SEVIRI filter functions are superposed, as in Figure 3.

column of Table 2). The optical properties are calculated using Mie theory and a five-mode lognormal size distribution [*Haywood et al.*, 2003, 2005]. Since it is commonly used by the remote sensing community, we also present results obtained using the standard dry desert dust model provided by the Optical Properties of Aerosol and Cloud (OPAC) database [*Hess et al.*, 1998]. As an extra sensitivity test, optical properties are recalculated for the WMO indices removing the contribution from the largest mode (geometric mean radius of 1.8 μm). Figure 4 shows the extinction coefficient normalized to 10 μm for each dust representation, again with the relevant SEVIRI filter functions superposed. For a given change in dust loading, the representation from the full mode WMO will produce the largest absolute T_B signal in the 10.8 μm channel and hence the greatest perturbation to the RGB blue signal. Removing the largest mode of this representation tends to reduce the normalized extinction coefficient in the 10.8 and 12.0 μm channels but has relatively little impact at 8.7 μm. The distinct spectral flattening of the extinction coefficient between the 10.8 and 12.0 μm channels in the OPAC representation relative to the other models tested here is particularly worthy of note.

[12] The spectral differences seen between the three sets of optical properties generated using the same size distribution can provide some indication of differences in dust composition. The Fouquart refractive indices were derived from sand samples taken from Niger, while the corresponding Volz data were obtained from samples of wind-blown Saharan dust deposited in Barbados. In both cases, the peak in the extinction coefficient at ~9.5 μm is a reflection of the presence of silicates although a preponderance of illite and kaolinite is also noted in the Barbados samples, both of which would also exhibit features within the 9–10 μm range [*Sokolik and Toon*, 1999]. The presence of these minerals would also be consistent with features seen in the single scattering albedo for the Volz, and, to a lesser extent, the WMO representation (not shown), although numerous other minerals (e.g., calcite, feldspar, and gypsum) reported in African dust samples [*Kandler et al.*, 2009] also absorb in this region. The OPAC desert dust model consists of a water-soluble mode [*Shettle and Fenn*, 1979] in combination with three larger size modes designed to capture mineral nucleation, accumulation, and coarse modes. These mineral components each have the same refractive indices, taken from a number of sources as described by *Koepke et al.* [1997] and intended to be broadly representative of a mixture of clay and quartz materials. The flattening of the extinction coefficient seen in the OPAC model between 10.8 and 12.0 μm is driven primarily by the refractive indices assumed in the model.

[13] To simulate the sensitivity to the vertical distribution of dust, loadings within an atmospheric profile are assumed to be constant with height, but the top of the dust layer is varied to be 1, 2, 3, and 4 km (fifth column in Table 2). While isolated events can certainly reach higher altitudes, this is a realistic range over which to test sensitivity based on CALIPSO observations [*Liu et al.*, 2008].

[14] In this section (given our focus on the IR and the variation in the relationship between visible and IR optical depths for each dust representation), the dust optical depth is defined at 10 μm (τ_{10} hereafter) and allowed to vary between 0.0 and 1.0 in steps of 0.1 (sixth column of Table 2). This corresponds to a maximum value at 0.55 μm which varies between ~2 and 8 dependent on the dust representation employed. Note that in all cases the use of Mie theory implicitly assumes that the particles are spherical, which is unlikely to be the case in reality. A recent theoretical analysis by *Hansell et al.* [2011] suggests that particle morphology can impact the mass extinction coefficient within the mid-IR, at least when considering single minerals. Whether such marked differences would be seen when considering mineral mixtures is less clear, but nevertheless the assumption of particle sphericity is a limitation of our study.

3.2. Simulation Results

[15] Table 3 indicates the mean, standard deviation, and range of T_{B087}, T_{B108}, and T_{B120}, and the relevant channel combinations obtained for the cases simulated here. Note

Table 3. Range, Mean, and Standard Deviation of Simulated SEVIRI Window Channel T_Bs and T_B Differences for Sensitivity Analysis[a]

Channel	Mean (K)	Minimum (K)	Maximum (K)	Standard Deviation (K)
T_{B087}	289.43	277.50	299.48	4.33
T_{B108}	293.24	284.98	299.94	3.66
T_{B120}	293.05	285.55	298.68	3.42
T_{B120}–T_{B108}	−0.19	−2.35	2.79	0.87
T_{B108}–T_{B087}	3.81	−0.41	11.18	2.66

[a]See Table 2 for the range of parameters used.

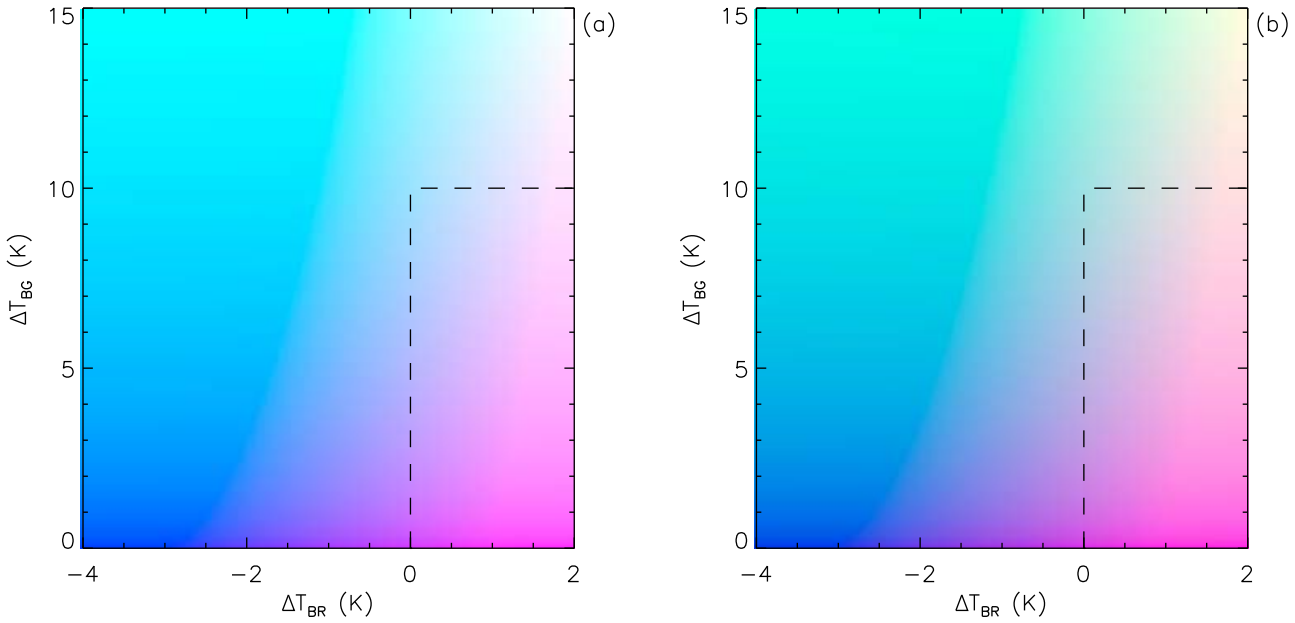

Figure 5. Two-dimensional graphical depiction of RGB rendering showing colors as functions of T_{B120}–T_{B108} (ΔT_{BR}) and T_{B108}–T_{B087} (ΔT_{BG}). (a) Blue channel set to saturation and (b) blue channel set to T_B = 285 K. Dashed lines show the criteria for dust detection suggested by Ashpole and Washington (submitted manuscript).

that T_{B108} exceeds 289 K in over 92% of the simulations, hence saturating the blue channel in the vast majority of cases. This saturation does typically occur for observed clear-sky conditions over the North African region (see section 4). The range of the T_B differences that constitute the red and green signals is broadly consistent with the maximum and minimum settings used to render the dust RGB images (Table 1).

[16] Given the tendency for the blue channel to saturate, it is possible to construct a two-dimensional plot showing how the dust RGB color will vary with T_{B120}–T_{B108} (hereafter ΔT_{BR}), and T_{B108}–T_{B087} (hereafter ΔT_{BG}), assuming that Int_B (equation (1c)) is equal to 255 (Figure 5a). One of the difficulties in assessing whether dust can be seen in the RGB imagery is because of the subjective interpretation. Automating the imagery, combined with a knowledge of the geographical region certainly helps in this regard, but detection will still vary from observer to observer. To try to circumvent this problem, I. Ashpole and R. Washington (An automated dust detection using SEVIRI: a multi-year climatology of summertime dustiness in the central and western Sahara, submitted to *Journal of Geophysical Research*, 2012) have developed an objective automatic algorithm, focusing on summertime conditions over northwest Africa. The black dashed lines in Figure 5a indicate ΔT_{BR} and ΔT_{BG} threshold values that they have derived on the basis of manual inspection of a large number of images. Their initial investigations suggested that the imagery could be considered dust contaminated when $\Delta T_{BR} \geq 0$ K, $\Delta T_{BG} \leq 10$ K, and $T_{B108} \geq 285$ K. This last threshold reduces the signal in the blue channel to below saturation; hence Figure 5b shows the color scheme that is obtained with T_{B108} set to 285 K. The reduction of the blue component means that the RGB image no longer turns white (top right-hand corner) but there is no obvious discernable visual change from the saturated case. Although there are clearly pink regions outside of the box, and a small turquoise area toward the top left-hand corner, to provide a consistent basis for our analysis here, we choose to use these thresholds as indicative of whether an observer would consider the RGB image "dusty" or not since, in general, pixels with values satisfying these thresholds will appear pink.

3.2.1. Sensitivity to Atmospheric Profile and Surface Type

[17] In Figure 6 results of selected simulations are superposed onto the color diagram shown in Figure 5a. In Figure 6a the black (white) triangles represent June 10:30 (05:30) UTC control conditions for barren soil (Table 2). In both cases, the most left-hand symbol corresponds to pristine conditions. ΔT_{BG} then reduces, while ΔT_{BR} increases as τ_{10} is increased. The stars and crosses are color coded in a similar way and show the effect of introducing 50% and 100% fractional vegetation cover, respectively. As the vegetation cover increases, the surface emissivity becomes less spectrally dependent (Figure 3) and the pristine-sky ΔT_{BR} and particularly ΔT_{BG} reduce. For each surface type, the atmospheric profile is the only difference between the black and white cases with the 05:30 UTC profile being slightly moister by 3.3 mm and cooler (surface temperature reduced by 5.2 K) than the 10:30 UTC case. Both of these differences act to reduce window T_Bs but have different spectral dependencies. For a spectrally flat surface emissivity, variations in surface temperature will tend to have the largest effect at 8.7 μm, reducing with increasing wavelength, while for a given change in total CWV the opposite is true with the largest impact at 12.0 μm [e.g., *Brindley and Allan*, 2003]. For the changes seen here, under pristine conditions with 100% vegetation cover the surface temperature effect dominates, and both ΔT_{BR} and ΔT_{BG} increase. With reduced vegetation cover the strong reststrahlen effects manifested in

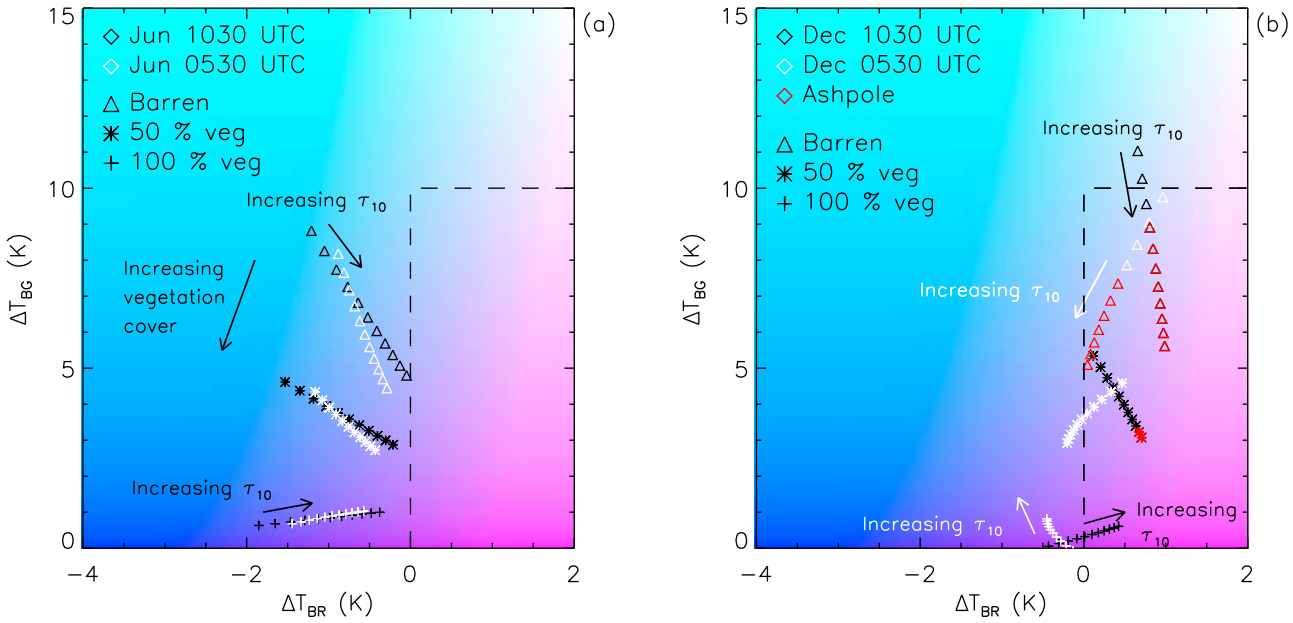

Figure 6. Sensitivity of RGB rendering to atmospheric profile and surface type. (a) June conditions and (b) December conditions at Niamey. Here τ_{10} is varied from 0.0 to 1.0 in steps of 0.1. Different symbols stand for different surface emissivities (see Table 2 for more details). Red symbols in Figure 6b mark where the method proposed by Ashpole and Washington (submitted manuscript) to ameliorate the effect of surface type flags dust (see section 3.2.1).

the surface emissivity play an increasingly important role such that ΔT_{BG} reduces in the 05:30 UTC relative to 10:30 UTC case. This, in conjunction with the fact that the dust representation used in these scenarios has slightly enhanced extinction at 10.8 μm relative to 8.7 μm (Figure 4), is the reason why the reduction in ΔT_{BG} with increasing τ_{10} also reduces with fractional vegetation cover, until, for 100% cover the behavior is reversed. Finally, the increased rate of change of ΔT_{BG} and ΔT_{BR} with τ_{10} in the 10:30 UTC relative to 05:30 UTC cases is a result of the enhanced lower tropospheric lapse rate in the former profile.

[18] Figure 6b is the corollary of Figure 6a for the December profiles. For 10:30 UTC essentially the same patterns of behavior are apparent, but there is an overall shift to higher values of ΔT_{BR} and a subsequent increase of "pinkness" in the RGB signal. This shift is a consequence of a fourfold reduction in the total atmospheric moisture content, from ~40 mm in June to ~10 mm in December, enhancing T_{B120} relative to T_{B108}. The moisture effect dominates over a small opposing effect resulting from the reduced surface and near-surface temperatures seen in the latter month. While the 05:30 UTC ΔT_{BG} and ΔT_{BR} values are also shifted, their behavior with increasing τ_{10} is strikingly different to the 10:30 UTC simulations. Here, the near-surface temperature inversion (Figure 2a), coupled with the enhanced dust extinction at 10.8 μm relative to 12.0 μm, results in a reduction of the ΔT_{BR} signal with increased τ_{10}, effectively reducing the pinkness of the signal.

[19] Looking at the positioning of the simulations in Figures 6a and 6b, it is clear that for conditions typical of Niamey in June, and with the control dust settings, high atmospheric moisture contents mask the dust signal and would preclude the detection of dust from the standard RGB imagery using the thresholds suggested above. For conditions similar to those seen during sunlit hours at Niamey in December, the automated approach would have an increased success rate, but could also potentially result in false detections. The presence of a surface inversion appears to confound the approach further, since it could lead to both false detections and miss higher dust loadings, particularly over partially vegetated surfaces. To try to ameliorate the influence of surface type, Ashpole and Washington (submitted manuscript) introduce a further test, which looks at the deviation in the ΔT_{BG} signal from the mean clear-sky ΔT_{BG} signal calculated over a rolling 15 day period prior to the given observation for each pixel. While this type of approach has, to the best of our knowledge, not been implemented thus far in other papers, which have used the dust RGB to develop climatologies, it is instructive to see whether it can help to remove instances of false detections. Here we use the true pristine-sky ΔT_{BG} as a proxy for the 15 day mean value. Points that pass both the threshold and anomaly tests (ΔT_{BG}–$\Delta T_{BGpris} \leq -2$ K) are marked in red in Figure 6b. The extra test tends to highlight cases with enhanced τ_{10}, but at least for these idealized simulations looks a little restrictive.

3.2.2. Sensitivity to Dust Optical Properties and Height

[20] Figure 7a provides an illustration of the sensitivity of the dust RGB color scale to dust top altitude for conditions corresponding to a barren surface type and WMO dust representation. As τ_{10} is increased, the dust layer becomes increasingly opaque, such that the influence of changes in dust top altitude is more apparent: effectively most of the IR signal within the relevant channels is coming from the dust layer itself. Because of the enhanced extinction seen within the 10.8 μm relative to the 8.7 and 12.0 μm channels for this dust model, ΔT_{BR} (ΔT_{BG}) shifts toward more positive (negative) values as dust top height increases, turning the

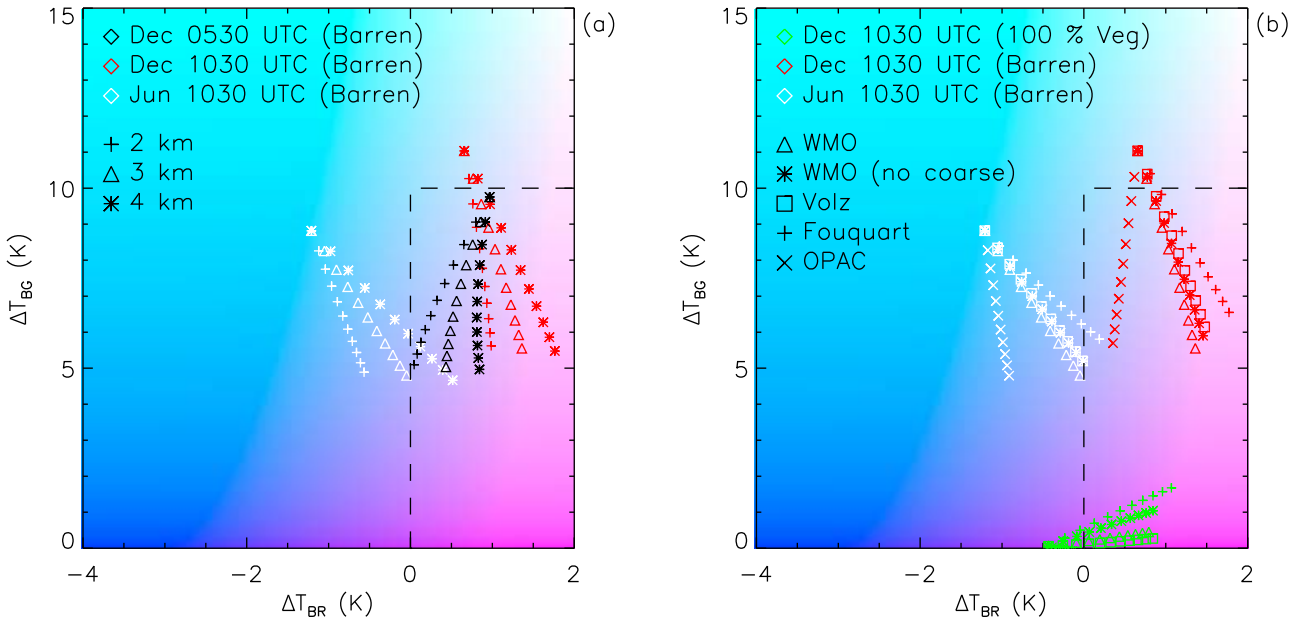

Figure 7. Sensitivity of RGB rendering to height of dust layer top and dust optical properties. (a) Variations of dust layer top from 2 to 4 km (symbols) for barren soils and different December and June conditions (colors). (b) Variations of dust optical properties (symbols) for differing meteorological and surface conditions (colors). See Table 2 for more details.

RGB signal steadily more pink. As noted previously, an increasing vegetation fraction eventually leads to an inversion in the behavior of the green component with τ_{10}, however, given this baseline, systematically increasing dust top altitude take ΔT_{BR} and ΔT_{BG} in the same direction as for the barren case (not shown).

[21] The role of dust properties in influencing the RGB signal is shown in Figure 7b. Again, as the dust layer becomes more opaque the impact of varying the dust properties becomes more marked. Over a barren surface the relatively enhanced extinction at 10.8 μm relative to 12.0 μm seen in the dust representation due to Fouquart (Figure 4) means that for a given τ_{10} these simulations will be more readily identified as dusty according to the criteria used here. Conversely, the flattening of the extinction coefficient between the 10.8 and 12.0 μm channels for the OPAC case means that the opposite is true for these simulations. For this surface type the T_B differences generated using the other two dust representations tend to cluster relatively closely together. There is also little sensitivity to the change in size distribution. With increasing vegetation cover, spectral differences in the dust properties over the 8.7 and 10.8 μm channels become more evident because of the flattening of the surface emissivity (Figure 3). This results in an enhanced response to the size distribution perturbation.

3.2.3. Sensitivity to Viewing Geometry

[22] Over the North African and Arabian regions the SEVIRI viewing zenith angle, θ_v, ranges from ~10 to 60° (Figure 8a). Because of the spectral dependency of atmospheric and dust extinction, the increase in atmospheric path length with increasing θ_v will influence the dust RGB signal. Figure 8b shows the impact of altering θ_v for December and June 10:30 UTC control conditions. Taking the latter case first, the differences due to increasing θ_v are as might be expected. For pristine conditions (top left points) the increase in path length manifests itself predominantly as an enhancement in water vapor absorption, hence reducing both ΔT_{BR} and ΔT_{BG}. While the trajectory with increasing τ_{10} is broadly similar for each θ_v, for a given step in τ_{10} at low dust loadings, the increments in ΔT_{BR} and ΔT_{BG} tend to be larger as θ_v increases because of the spectral extinction properties of the dust layer. With increasing dust loading the sensitivity of the increments in ΔT_{BR} and ΔT_{BG} to θ_v is reduced as the channels begin to saturate. For the December conditions the results are perhaps less easy to interpret. Here, while an increasing path length takes the pristine ΔT_{BR} in the expected direction, ΔT_{BG} actually increases. The reason is that in this case the water vapor content of the atmosphere is sufficiently low that the contribution of other atmospheric absorbers is more critical in driving the θ_v response. Because the 8.7 μm channel is more strongly affected by these minor gases than the longer wavelength channels T_{B087} shows a more rapid decrease with θ_v. As dust is introduced into the atmosphere the relative response mimics that seen for the June case for the same reasons discussed above. The results indicate that the water vapor content of the atmosphere is the main factor in determining whether an increase in θ_v will strongly affect the ability to identify dust in the RGB imagery.

3.3. Synthesis

[23] The sensitivity tests described in section 3.2 imply that, for a given τ_{10} and surface type the largest influence on the RGB signal is CWV. Dust mineralogy can have a sizable effect via its impact on the composite refractive index, but changes to the size distribution, at least for the cases considered here, appear to have a lesser effect. Dust altitude, whose impact is implicitly linked to the lower tropospheric lapse rate, has an effect of a similar magnitude to that of dust composition. Altering the surface type has a sizable impact

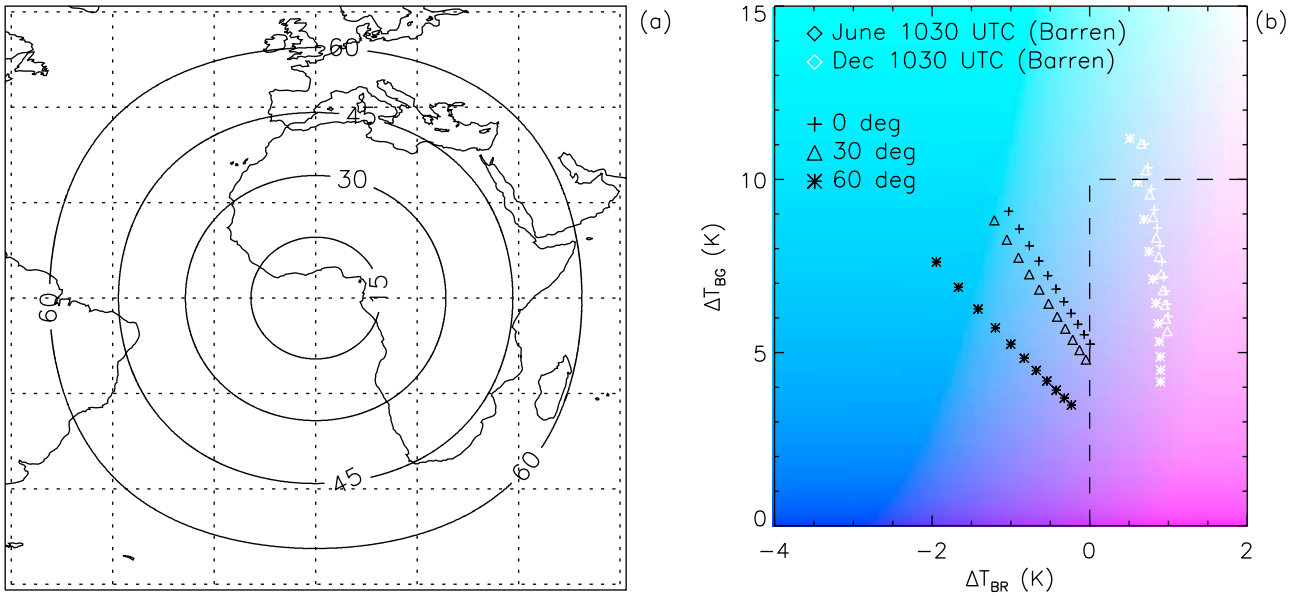

Figure 8. Sensitivity of RGB rendering to viewing zenith angle. (a) Horizontal map showing viewing geometry for Meteosat-9. (b) Effects of variations of the zenith angle on dust detection (symbols) for barren soils and December and June conditions (colors). See Table 2 for more details.

on the actual T_B differences comprising the red and green channels, but, from these simulations, appears to only markedly alter the τ_{10} at which the RGB signal turns pink when total column water vapor amounts are low. CWV also plays a key role in determining the impact of variations in viewing zenith angle on the RGB signal.

4. Application to Observations: The Case Study of 3 June 2006

[24] Having obtained a theoretical understanding of how key factors influence the dust RGB rendering scheme, in this section we highlight a specific case study to assess whether our inferences are correct. We focus on 3 June 2006, an example from the first SAMUM field campaign [*Heintzenberg*, 2009] in southern Morocco, for which detailed lidar, Sun photometer, and radiosonde measurements are available. Meteorological conditions on 3 June 2006 and the previous days are described in detail by *Knippertz et al.* [2009] (hereinafter K09; their case I). This period was characterized by the widespread mobilization of dust across northeastern Algeria, which was subsequently mixed vertically and transported into southern Morocco. More dust was emitted locally in connection with cold pools from deep moist convection over the Atlas Mountains [*Knippertz et al.*, 2007]. The analysis is divided into two steps. In section 4.1 geographical distributions of temperature and moisture taken from operational analyses by the European Centre for Medium-Range Weather Forecasts (ECMWF) are used to generally assess the probability of dust detection for the synoptic conditions on 3 June. In section 4.2 detailed point measurements from the two SAMUM sites at Ouarzazate and Tinfou are used to provide a more constrained assessment of our ability to capture the behavior of observed SEVIRI 8.7, 10.8, and 12.0 μm brightness temperatures.

4.1. Geographical Distributions

[25] For the region 14°W–34°E, 8–36°N, Figure 9 shows geographical distributions of CWV and lapse rate, expressed here as the temperature difference between the surface and the top of the dust layer, which for the sake of simplicity was assumed to lie at 2 km above ground level (agl), on 3 June 2006 at 06:00 and 12:00 UTC on the basis of 1° resolution operational ECMWF analyses. Because of the strong radiative cooling of the surface during the night, temperature differences range between −10 and +10 K over most of the domain at 06:00 UTC with very stable conditions over the SAMUM region (Figure 9a). Higher values are observed over parts of the relatively warm Mediterranean Sea and in the east of the domain, where the sun rises earlier. At midday, temperature differences exceed 35 K over the desert and range around 20 K in the Sahel (Figure 9b). Changes from morning to midday are generally small over water. As expected, the corresponding CWV distributions show much less temporal variation (Figures 9c and 9d), with a marked increase as one moves south toward the Sahel. Over the Sahara values vary from below 10 mm over Algeria, Egypt, and Sudan to more than 25 mm over Libya. Southern Morocco is relatively moist with a CWV around 20 mm.

[26] Subsampling these profiles at 2° × 2° resolution, assuming a θ_v of 20°, and varying the 0.55 μm optical depth (τ_{055} hereafter) from 0.0 to 1.0 in steps of 0.2, simulations were performed using the surface emissivities for barren soil and 50% vegetation cover (Figure 3), dust properties derived from the Volz refractive indices (Figure 4), and the *Haywood et al.* [2003, 2005] size distribution. For the sake of brevity, only results for τ_{055} = 0.0, 0.4, and 1.0 are displayed in Figure 10. Crosses show 1200 UTC simulations, and triangles show 06:00 UTC. Figure 10 provides an illustration of the success of the pink imagery as a function of lapse rate and CWV as judged using the ΔT_B and T_B

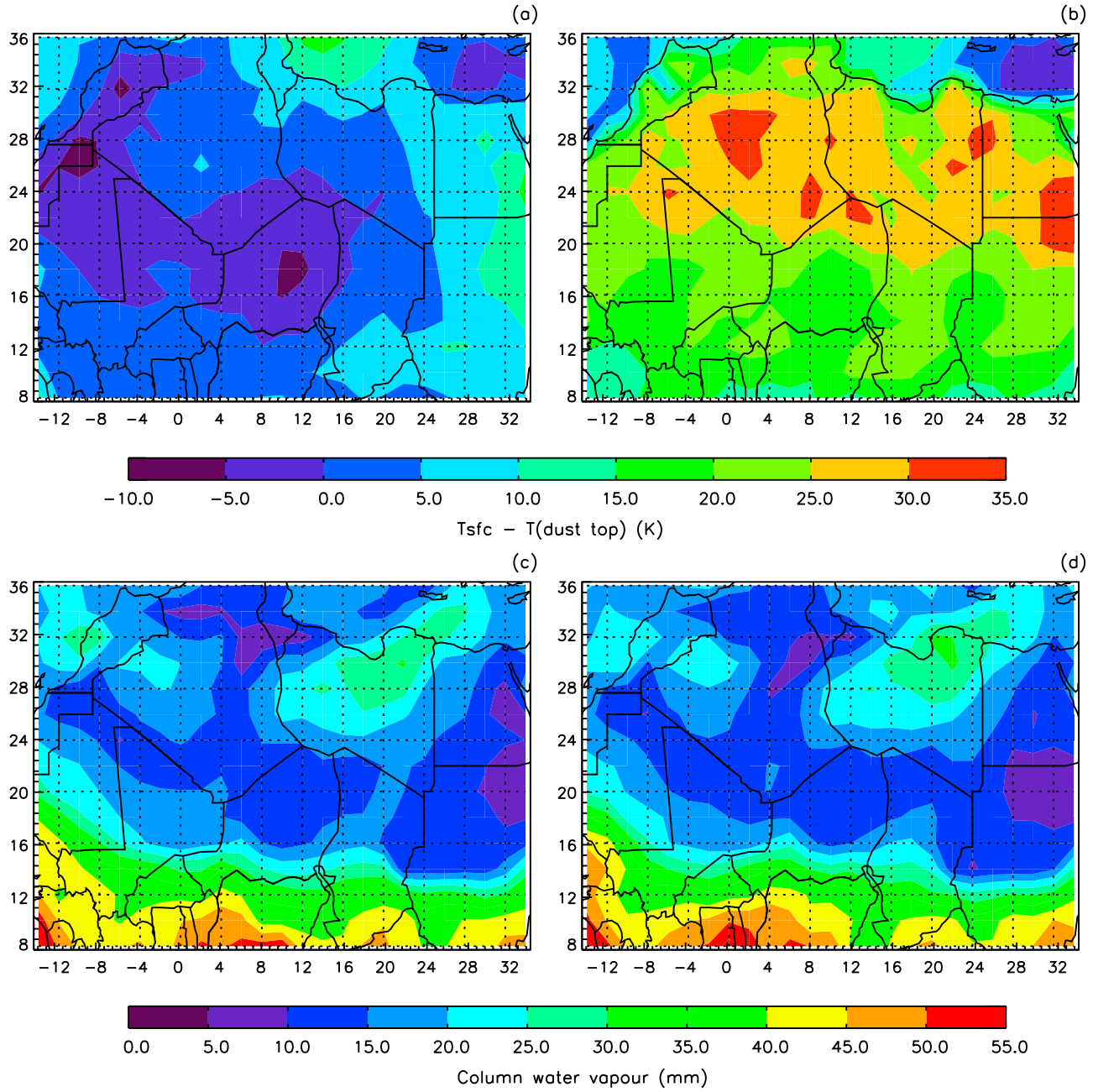

Figure 9. Case study for 3 June 2006: Synoptic conditions over northern Africa. Temperature differences between the surface and the top of the dust layer (assumed to be at 2 km above ground level (agl)) for (a) 06:00 UTC and (b) 12:00 UTC. (c and d) The same for column water vapor (CWV). Data are taken from European Centre for Medium-Range Weather Forecasts operational analyses at 1° × 1° horizontal resolution.

thresholds described in section 3.2. If the symbols are black, then the RGB product would not have identified dust. Red symbols indicate that a detection has been made.

[27] Looking at the pristine case, it is clear that the detection gives false results for a number of 06:00 UTC profiles (Figures 10a and 10b) with more false detections over partly vegetated areas, even at very low CWV. These tend to occur preferentially when there is a marked temperature inversion, similar to the results seen in section 3.2.1, although there is no obvious set of temperature and CWV values that could be used to isolate these cases.

[28] Turning to the panels where dust is present in the simulations (Figures 10c–10f), at first sight the results are rather curious. Excluding those 06:00 UTC cases which were falsely flagged as dusty when pristine, there appears to be a cutoff value of total CWV of ~25 mm for barren soils, above which the pink imagery does not identify dust no matter what the temperature profile (Figures 10c and 10e). Below this value, for a given total CWV, dusty points are

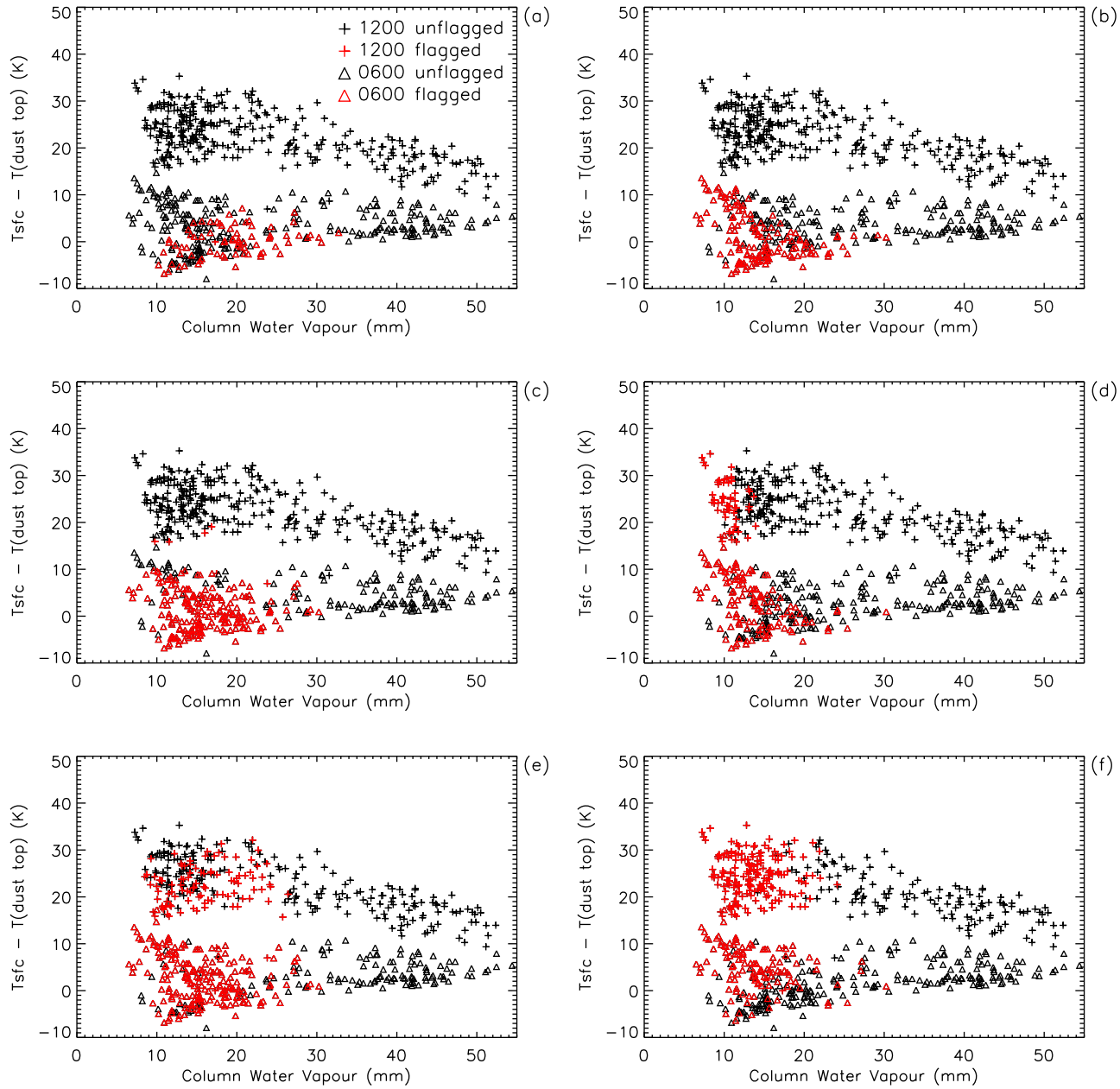

Figure 10. Case study for 3 June 2006: Capability of the RGB product to detect dust under realistic atmospheric conditions. All plots show temperature differences between the surface and the top of the dust layer (assumed to be at 2 km agl) versus CWV for 06:00 (triangles) and 12:00 UTC (crosses). Data points that would fall into the thresholds indicated by the dashed lines in Figure 5 are marked in red. The 0.55 μm optical depth τ_{055} = 0.0 for (a) barren and (b) 50% vegetated surface. (c and d) Same as Figures 10a and 10b, but for τ_{055} = 0.4. (e and f) Same as Figures 10a and 10b, but for τ_{055} = 1.0.

preferentially identified in profiles with a lower temperature lapse rate, contrary to what might have been expected from section 3.2.2. The reason for this becomes apparent when considering the analogous results for a partially vegetated surface (Figures 10d and 10f). These results are much closer to what we might have anticipated from the Niamey-based simulations (see section 3.2), with a tendency for dust to be successfully flagged at lower values of τ_{055} in profiles with higher lapse rates at a given CWV. The cutoff value in CWV is also shifted a little lower to ~20 mm at $\tau_{055} \leq 1$. Figure 11 shows which tests result in the failure of the dust flag at τ_{055} = 1.0 for the barren and partially vegetated surface, respectively. Essentially, for the barren surface, at high temperature lapse rates and low total CWV the low surface emissivity in the 8.7 μm channel causes the ΔT_{BG} signal to exceed 10 K (Figure 11a). When the feature is partially obscured by vegetation values are suppressed below the 10 K threshold (Figure 11b). The reduction in the cutoff column moisture value in the partially vegetated case is because of the flattening of the emissivity spectrum between 10 and 12 μm compared to barren conditions (Figure 3).

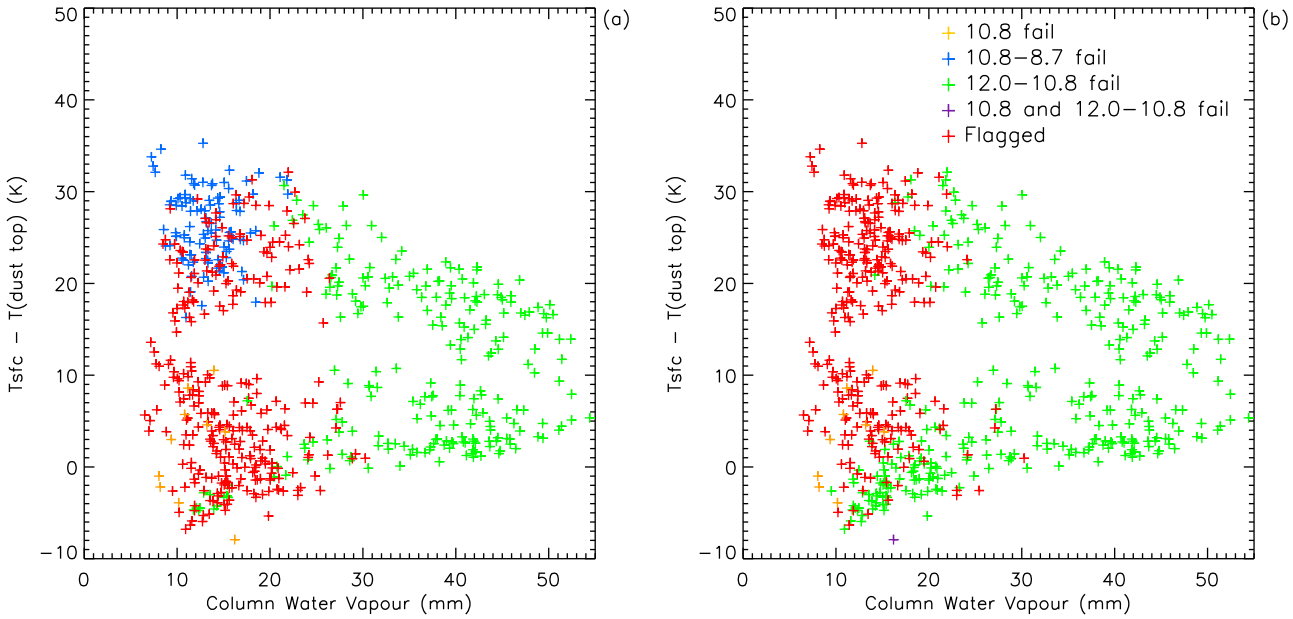

Figure 11. Case study for 3 June 2006: Same as Figures 10e and 10f, but all symbols were replaced by crosses with colors indicating which parameter prevented the flagging of a given profile, as detailed in the legend.

[29] How might these findings affect our ability to diagnose dust on the basis of the RGB imagery? Figure 12 shows the June 2006 monthly surface emissivity at 8.3 μm derived from a combination of MODIS observations and measured emissivity spectra [*Seemann et al.*, 2008]. Highest emissivities with values above 0.9 are found over the vegetated areas of southern West Africa and along the Mediterranean coast, while large parts of the Sahara show emissivities well below 0.8. Mountainous areas such as the Hoggar, Tibesti, or Aïr stand out as having higher values. The pattern for 8.7 μm can be expected to be very similar (see Figure 3). Stars (squares) in Figure 12 indicate where a false detection would have been made at 06:00 UTC assuming a barren (partly vegetated) surface type. When both symbols are present, a false detection would have made irrespective of surface type. Ideally, we would like to see an absence of stars over regions of low emissivity and an absence of squares over regions of higher emissivity. The former is generally the case, apart from an area over central western Algeria and central Mauritania. The latter condition is generally not met, with large parts of the central and eastern Sahara covered with squares. In addition, there is an extensive region over the northwestern Sahara and the Sahel in Niger and Chad, where a false detection would have been made irrespective of the chosen surface type. These areas tend to exhibit negative lapse rates as shown in Figure 9a. Under pristine conditions this results in an enhanced signal from the more opaque 12.0 μm relative to the 10.8 μm channel, resulting in a false detection. This analysis suggests that the imagery would turn pink over a large portion of northern Africa, even when no dust is present.

[30] Figure 13a shows the SEVIRI RGB image for 05:00 UTC 3 June 2006. Large areas of the Sahara and also its surroundings appear pink and it is not possible to clearly distinguish whether this indicates a true or false dust detection. In contrast, because of the enhanced surface temperature and lapse rate around midday (see Figure 9b), the imagery turns more bluish at 11:15 UTC (Figure 13b), and a dust event over Mali occurring at this time can be clearly detected. Retrievals from the Moderate Resolution Imaging Spectroradiometer (MODIS) at 13:35 UTC on the same day, obtained using the Deep Blue algorithm [*Hsu et al.*, 2004], indicate τ_{055} values in excess of 1.0 in this region (not shown).

[31] While our inferences concerning the potential for false detections appear to be corroborated by these observations, it is useful to consider a larger number of images to assess the overall representativeness of the simulations performed here. Accordingly, Table 4 provides information concerning the number of SEVIRI observations made at 06:00 UTC and 12:00 UTC through June and December 2006 that fall within the simulated range of values over the region 25°W to 65°E, 0 to 40°N, considering land points only. Despite the fact that the simulations performed here are limited to using analyses from one day of June 2006, one dust representation, and two surface emissivities, they encompass a large percentage (in excess of ~70%) of the observations made during June at 06:00 and 12:00 UTC, and December at 12:00 UTC. Outliers at these times are mainly related to the presence of optically thick clouds, which reduce the brightness temperatures in all three window channels, coupled with a simulated green signal which is slightly too high compared to the observations. This latter issue is likely related to the assumed surface spectral emissivity, which, for the barren and 50% vegetated cases considered here, shows enhanced 10.8 relative to 8.7 μm values (Figure 4). This may not be true for certain geographical areas within the region of interest such as Yemen and Oman.

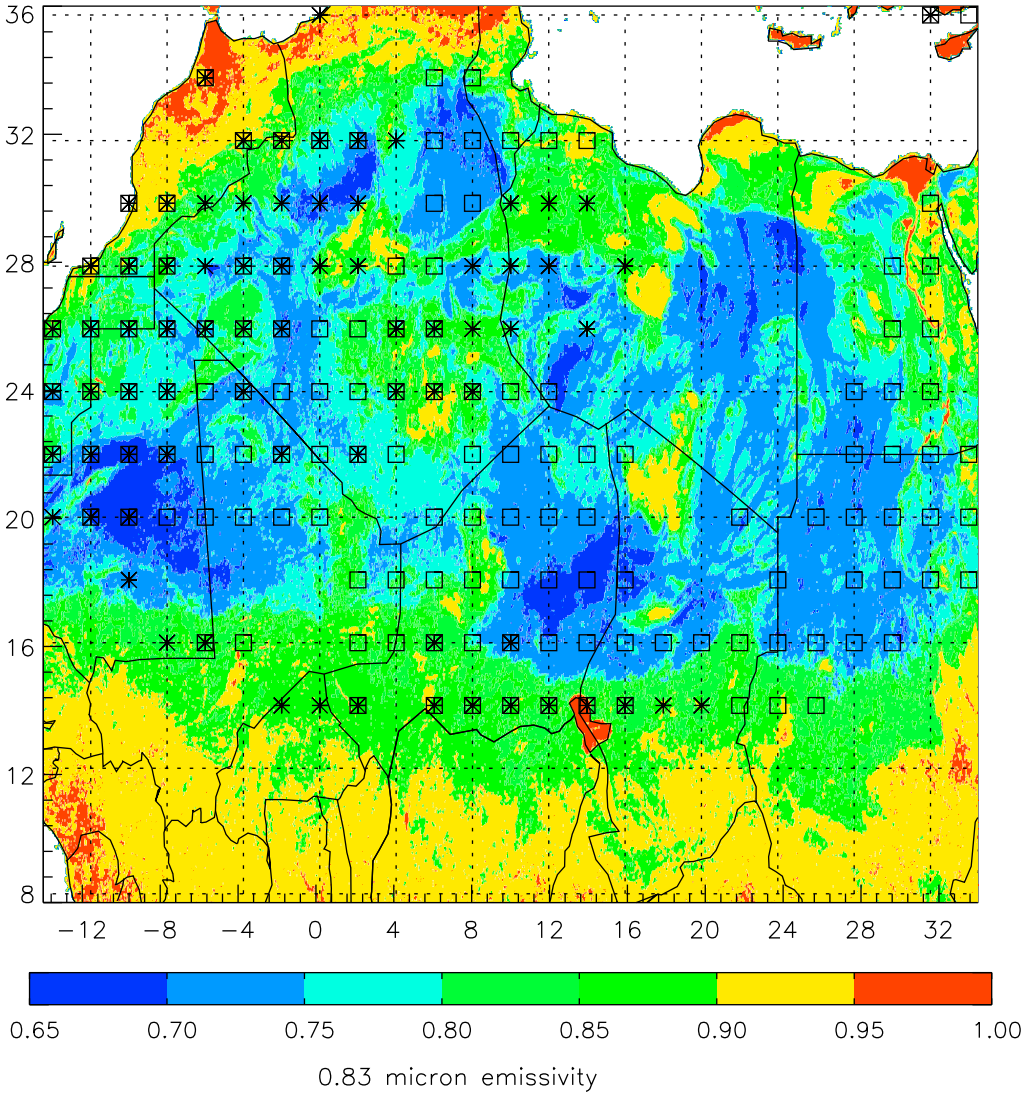

Figure 12. Case study for 3 June 2006: Geographical map of surface emissivity at 8.3 μm. Symbols every 2° longitude and latitude show where false detections of dust would have been made using the atmospheric profiles at 06:00 UTC. Stars (squares) indicate false detection assuming barren (50% vegetated) soil, i.e., low (medium) emissivity. Both symbols indicate false detection for both soil types.

[32] The ability of our simulations to capture the observed behavior is clearly reduced at 06:00 UTC through December 2006. Here the main issue appears to be markedly lower observed brightness temperatures in the 10.8 and 12.0 μm channels, a consequence of the skin and near-surface temperatures at this time being significantly colder than those used in the simulations (not shown). Colder values in both the 10.8 and 12.0 μm channels would actually tend to turn the dust RGB composites more pink/red in general (compare Figures 13a and 13b which essentially illustrate this effect) and make dust events more difficult to discriminate visually, in agreement with our findings concerning the increased likelihood of false detections in the early morning hours. However, it should be reiterated that the automated detection thresholds we have employed here were developed specifically for summertime over northwest Africa. These results suggest that they would likely need adjusting at least as a function of time of day to perform reliably throughout the year.

4.2. Detailed Point Measurements

[33] On 3 June 2006 Sun photometer, horizontal visibility, and lidar observations at the two SAMUM sites Ouarzazate airport (30.93°N, 6.90°W, 1133 m) and Tinfou (30.25°N, 5.62°W, 680 m); marked by white dots in Figure 13) indicate elevated levels of dust (Figures 2 and 6 in K09). Radiosondes were launched from Ouarzazate around 05:05 UTC and 11:15 UTC that day, and the temperature and dew point temperature profiles obtained are displayed in Figure 14. These combined sources of information can be used as input for radiative transfer simulations to assess whether we are able to match colocated SEVIRI observations given realistic uncertainties in each parameter, and to provide additional confirmation concerning our understanding

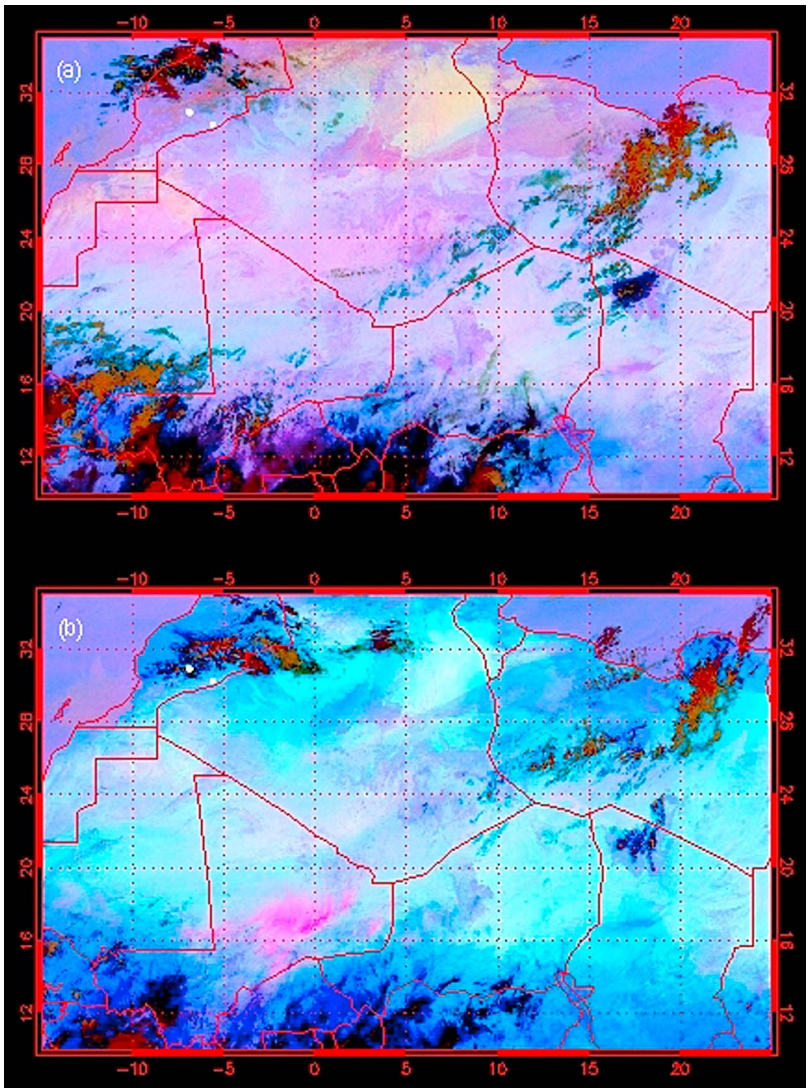

Figure 13. Case study for 3 June 2006: SEVIRI dust RGB images for (a) 05:00 UTC and (b) 11:15 UTC. The locations of the Saharan Mineral Dust Experiment (SAMUM) measuring sites in southern Morocco, Ouarzazate and Tinfou (close to Algerian border), are marked by white dots.

of the key variables influencing the ability of the RGB imagery to highlight dust.

[34] Dust layer top altitude can be derived from lidar observations at Ouarzazate. Before sunrise, two distinct dust layers exist that result from differential advection during the night (K09). The two layers can also be distinguished in the temperature profile with the upper one capped by a weak inversion around 616 hPa separating it from the dry mid-troposphere (Figure 14). For the sake of simplicity, in the simulations this profile will be treated as one homogeneous layer with a top at 4.3 km above sea level (asl). The temperature at this level according to the radiosonde from 05:05 UTC is 272.9 K (Figure 14). The low solar altitude at this time precludes Sun photometer measurements of

Table 4. Percentage of Observed SEVIRI Window Channel T_{BS} and T_B Differences Falling Within Simulated Value Ranges Through June and December 2006 at 06:00 and 12:00 UTC[a]

Month and Time	T_{B087}	T_{B108}	T_{B120}	$T_{B120} - T_{B108}$	$T_{B108} - T_{B087}$	All Channels
June, 06:00 UTC	88.3	84.5	82.7	86.8	69.6	64.0
June, 12:00 UTC	90.9	88.6	86.7	86.6	79.6	71.0
December, 06:00 UTC	69.5	54.3	55.7	95.3	60.0	29.7
December, 12:00 UTC	84.7	82.5	81.0	96.7	87.7	76.6

[a]A simultaneous set of observations across all channels and differences must fall within the simulated ranges to be included in the "all channels" percentage.

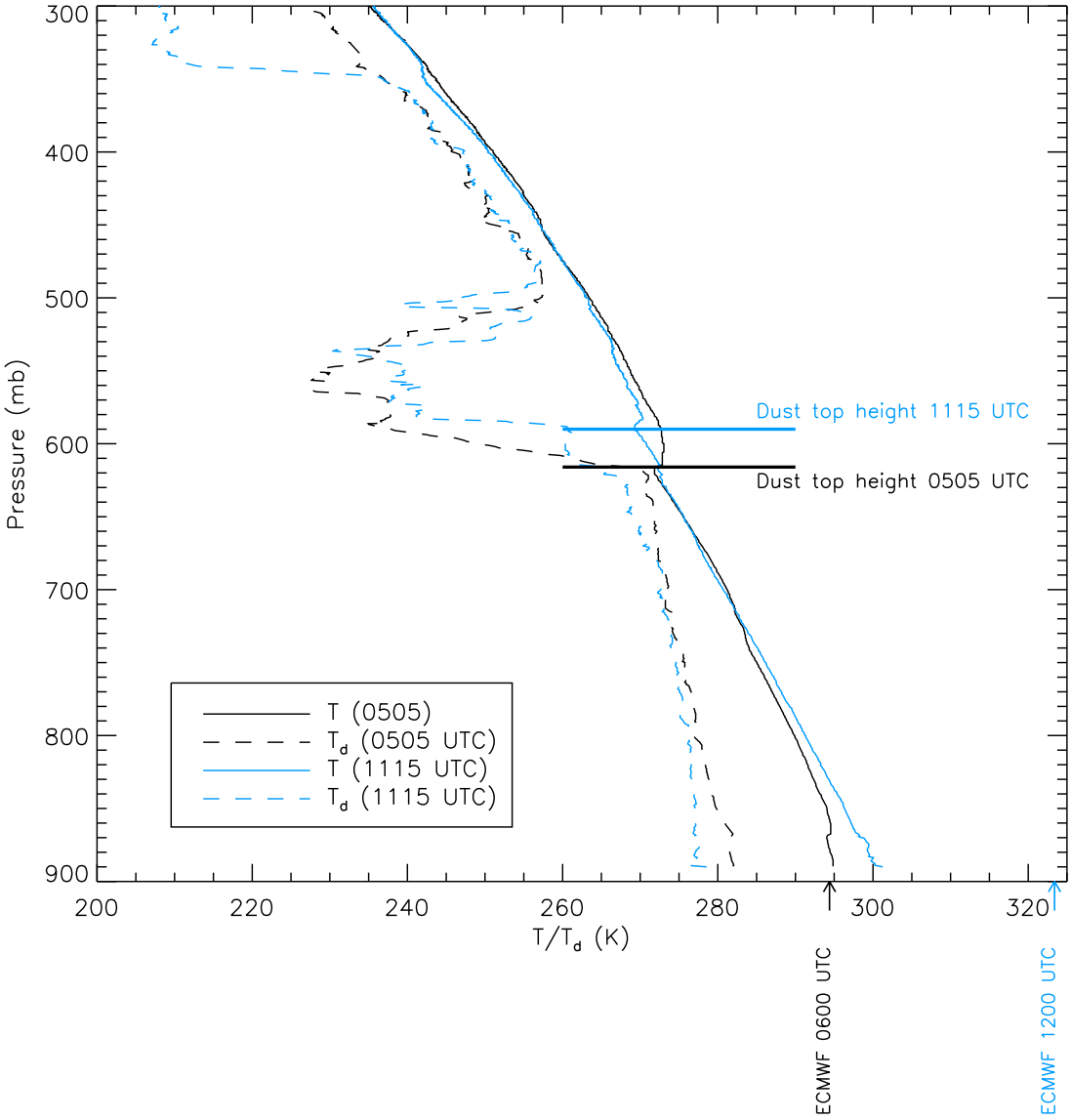

Figure 14. Case study for 3 June 2006: Vertical profiles of temperature and moisture used for simulation in section 4.2. The profiles are taken from rawinsonde launches from Ouarzazate airport at 05:05 and 11:15 UTC.

optical depth. However, although it has known limitations [*Horvath*, 1971] we can use the Koschmieder equation to obtain a rough estimate of τ_{055} from the horizontal visibility measurements at Tinfou. Here

$$\text{visibility} = \frac{\ln(50)}{K_{ext055}} \tag{3a}$$

where K_{ext055} is the extinction coefficient at 0.55 μm in m^{-1}. For a vertically homogeneous layer of thickness, δz, this translates to

$$\tau_{055} = \frac{\ln(50)\delta z}{\text{visibility}} \tag{3b}$$

At 05:05 UTC visibility at Tinfou is ~20 km. Since the height of the dust top above the ground is 3.62 km this suggests a value for τ_{055} in the region of ~0.7.

[35] As the morning progresses, the dust layer becomes increasingly mixed in the vertical in response to the destabilizing effect of solar heating, reaching a height of ~4.4 km asl (590 hPa) by 11:15 UTC with the lidar and radiosonde indicating mixing of dry, clean and moister, dusty air at the top (Figure 14). The temperature at this level is 269.4 K. τ_{055} observed by Sun photometer at Tinfou reaches a value of ~0.8 in the late morning. Optical depths at Ouarzazate are generally lower with a maximum value of ~0.5. Supplementing the radiosonde profiles with ECMWF analyses above 250 hPa and integrating over the vertical gives CWV amounts of 20.4 and 18.5 mm at 05:05 and 11:15 UTC, respectively (Table 5), which is consistent with Figures 9c and 9d.

[36] A parameter more difficult to determine is the skin temperature. Here we compare estimates from operational ECMWF analyses (marked in Figure 14) for the grid point nearest to Tinfou (30°N, 6°W) with those computed from

Table 5. Parameter Settings for the Radiative Transfer Simulations Over Tinfou on 3 June 2006[a]

Time (UTC)	Dust Top Altitude (km Above Sea Level)	Dust Top Temperature (K)	Column Water Vapor (mm)	T_{SKIN} (K)	$T_{SKIN} - T_{DUSTTOP}$ (K)
05:05	4.3	272.9	20.4	293.4 (E)	19.5
	4.3	272.9	20.4	298.2 (G)	25.3
	4.3	272.9	20.4	296.2 (S)	23.3
11:15	4.4	269.4	18.5	321.4 (E)	52.0
	4.4	269.4	18.5	323.2 (G)	53.8
	4.4	269.4	18.5	316.2 (S)	46.8

[a]In each case, τ_{055} was varied from 0.0 to 1.0 in steps of 0.2, using the dust properties derived as described in the text. T_{SKIN} estimates are from ECMWF operational analyses (E), ground-based IR retrievals (G), and soil temperature measurements (S).

ground-based broadband thermal IR measurements made at Ouarzazate airport as part of SAMUM [*Bierwirth et al.*, 2009] and from soil temperature observations made at surface stations from the Integratives Management-Projekt für einen Effizienten und Tragfähigen Umgang mit Süßwasser in Westafrika (IMPETUS) network [*Schulz et al.*, 2010]. Here we concentrate on the three stations Trab Labied (TRB, 31.17°N, 6.58°W, 1383 m asl), Argioun (ARG, 30.65°N, 6.32°W, 1020 m asl), and El Miyit (EMY, 30.36°N, 5.63°W, 792 m asl) in the surroundings of Ouarzazate and Tinfou. These stations have temperature measurements at 5, 15, and 30 cm depth every 15 min. A damping depth for the diurnal temperature wave was estimated for each station by regressing the logarithm of the diurnal amplitude of 3 June 2006 against depth. The skin temperature was then estimated via the dependence of the amplitude and phase on the damping depth.

[37] For 06:00 UTC the skin temperature from ECMWF analyses and SAMUM IR measurements are 293.7 and 299.2 K, respectively. Taking the typical diurnal cycle into account, we reduced these by 1°C to get estimates for 05:05 UTC. Estimates from the IMPETUS stations range from ~294 K in TRB and ARG to 302.2 K in EMY and were averaged to give 296.2 K. A corresponding analysis for 11:15 UTC gives 321.4 K (ECMWF), 323.2 K (SAMUM), and 316.2 K (IMPETUS). Despite the substantial differences, all three 11:15 UTC estimates show an extremely superadiabatic near surface layer. The marked range in skin temperature, coupled with the assumptions regarding dust altitude and profile shape, lead to relatively large uncertainties in skin minus dust top temperature.

[38] Despite the substantial dust loadings indicated by the horizontal visibility and Sun photometer measurements discussed above, the SEVIRI RGB images for the respective times do not show any indication of pinkness over southern Morocco (Figure 13). We can use our simulations from section 4.1 to understand this result better. The surface emissivity at 8.3 μm over southern Morocco shown in Figure 12 is more akin to values seen in the 50% vegetated emissivity spectrum than the barren case, so that we will concentrate on Figures 10d and 10f for the rest of this discussion (recall that those results are for a dust layer top of 2 km). For 05:05 UTC, lapse rates of ≥20 K and a CWV of ≥20 mm are clearly not detectable for τ_{055} = 0.4 and very marginal for τ_{055} = 1. The results indicate that the relatively high CWV is an important factor in concealing the dust signal. For 11:15 UTC, the CWV is slightly reduced and the lapse rate is at the upper end of the range plotted in Figure 11, both of which should assist in detecting dust. To answer why it is not apparent in the imagery further simulations are required.

[39] Figure 15 shows simulated 8.7, 10.8, and 12.0 μm T_Bs as a function of τ_{055} using the information summarized in Table 5. In both cases dust optical properties are calculated using Mie theory assuming refractive indices after *Volz* [1973] and the modified OPAC [*Hess et al.*, 1998] size distribution described by *Kandler et al.* [2009], appropriate to the SAMUM conditions. Horizontal dashed lines show the SEVIRI observations nearest to Tinfou. For 05:05 UTC the skin temperature from ECMWF is clearly too cold (Figure 15a), while the IMPETUS value also appears to be colder than would be inferred from SEVIRI assuming our estimate of τ_{055} is reasonable. Using the IR retrieved skin temperature value (Figure 15c), in combination with the partially vegetated surface appears to give more realistic results, with best agreement between the simulations and observations reached at τ_{055} ~0.6, close to our inferred value of 0.7.

[40] At 11:15 UTC, all three sets of simulations fail to match the observations (Figures 15d–15f), strongly suggesting an underestimation of the skin temperature, even by the ground-based IR measurements. Indeed, even assuming a perfect blackbody emitter and pristine conditions, the simulated T_Bs using the ECMWF and IMPETUS skin temperatures are lower than those measured from space. The difference in scales between the point measurements, satellite observations, and model reanalysis fields coupled with the larger spatial variability seen at this time compared to earlier in the day (Table 5) may go some way toward explaining this discrepancy. For the purposes of detection, what should be noted is that a change in skin temperature merely tends to shift all channel values up or down by a certain amount and does not substantially alter the point at which the imagery would turn pink. At 11:15 UTC the simulations suggest a dust optical depth of >0.8 would be required for Tinfou to be classified as dusty according to the criteria employed here, a loading just in excess of the measured value. In all six simulations, while ΔT_{BG} is below 10 K for the partially vegetated surfaces, negative 12.0 minus 10.8 μm values explain why the observations fail the automated pink detection criteria (see Figure 5).

5. Conclusions

[41] In this study we have performed, to the best of our knowledge, the first rigorous assessment of the strengths and limitations of SEVIRI RGB dust imagery, a tool commonly used to provide a proxy measure of dust presence for a wide variety of applications. We have performed a number of

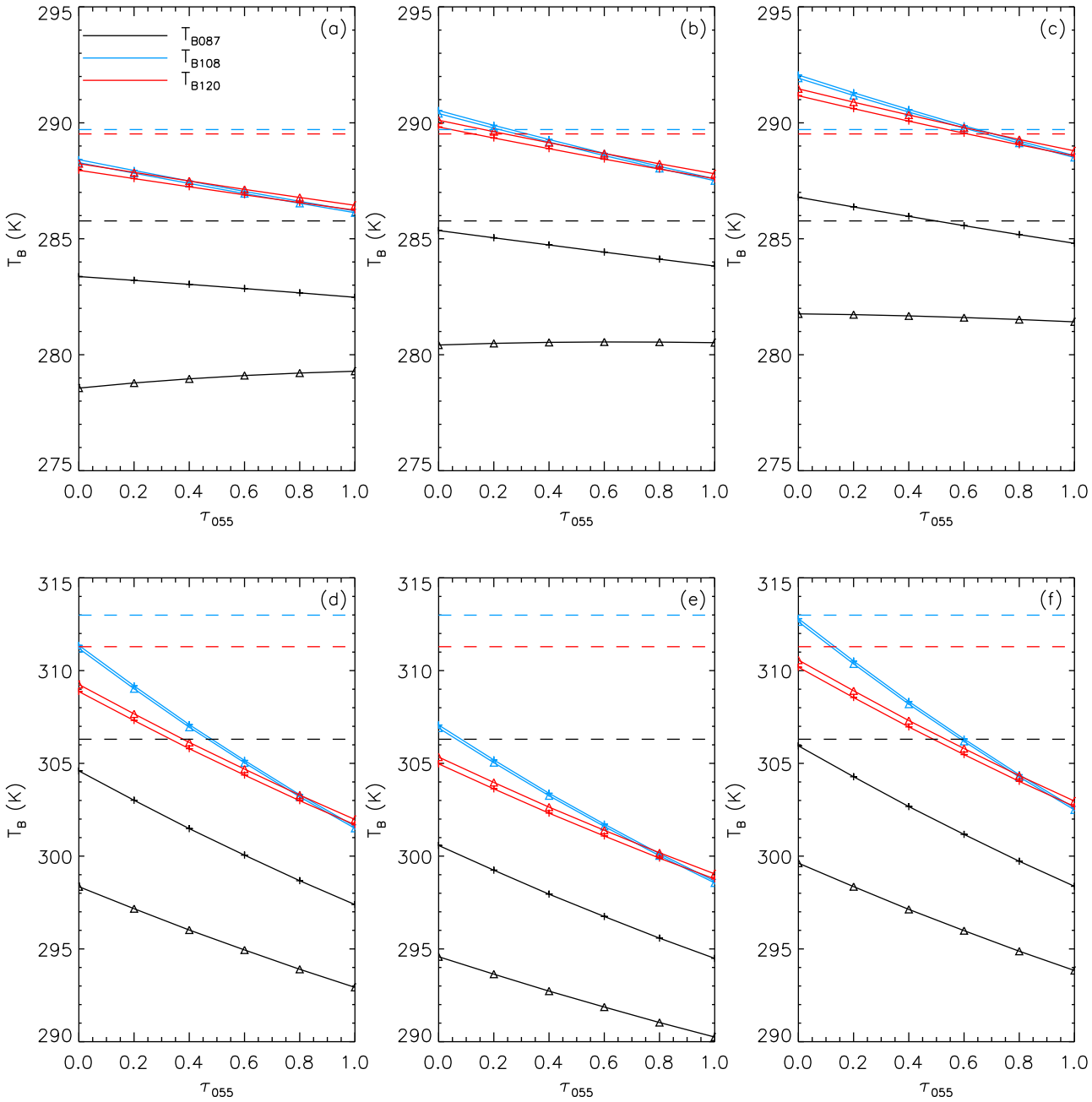

Figure 15. Case study for 3 June 2006: Matching of SEVIRI observations with available ground-based measurements (see Table 5). All plots show simulated T_Bs for the three SEVIRI channels used in this study plotted against τ_{055} with the observed values as horizontal dashed lines. Triangles and crosses indicate barren and 50% vegetated soil, respectively. Data for 05:05 UTC (a) using skin temperatures from ECMWF analyses and estimated from (b) IMPETUS soil temperatures and (c) SAMUM ground-based broadband thermal IR measurements, respectively. (d–f) Same as Figures 15a–15c but for 11:15 UTC.

dedicated idealized simulations using a range of realistic scenarios derived by combining observations of the atmospheric state in the target region, typical dust properties and surface conditions, and the characteristics of the SEVIRI instrument and satellite platform. We have also assessed whether similar modeling efforts are able to match the brightness temperatures observed within the SEVIRI mid-IR window channels used to generate the imagery given colocated measurements of the atmospheric profile, dust loading, and vertical distribution for a specific case study from the SAMUM campaign.

[42] We find that during daytime and early morning, over the North African region the thresholds used in creating the RGB imagery typically result in the blue channel (10.8 μm) saturating. This means that the degree of pinkness seen in the imagery is effectively controlled by the signals within the red (12.0 minus 10.8 μm) and green (10.8 minus 8.7 μm) channels, and enables the visualization of the response seen

to specific perturbations on 2-D color maps. It also suggests that it may be possible to use thresholds to objectively diagnose pinkness as suggested by Ashpole and Washington (submitted manuscript). However, changes in the underlying surface can strongly affect the signal in the green channel in particular. Over quartz-rich surfaces typical of sand seas the signal in the green channel will be large if the atmosphere is relatively pristine, but will reduce with enhanced dustiness, increasing the pinkness of the overall RGB image. Over rockier or partially vegetated terrain the signal in the green channel will be reduced even when little dust is present in the atmosphere, resulting in these regions having a pinker baseline appearance, particularly if the overlying atmosphere has low CWV. This can lead to pristine scenes being incorrectly identified as dusty using an objective approach.

[43] Systematic experiments show that, for a given dust amount and spectral surface emissivity, the largest influence on the RGB signal is CWV. Dust mineralogy can have a sizable effect via its impact on the composite refractive index, but changes to the size distributions considered here appear to have a lesser effect. Dust altitude, whose impact is implicitly linked to the lower tropospheric lapse rate, has an effect of a similar magnitude to that of dust composition, while the sensitivity to satellite viewing angle becomes more significant with enhanced atmospheric opacity. Both the idealized simulations and the case study results suggest that if CWV exceeds ~20–25 mm the pink signal will be masked even in the presence of substantial dust loading (τ_{055} up to ~0.8). For typical daytime lapse rates, increasing the dust top altitude enhances the pinkness of the signal because of the contrast between the surface emission and that from the dust top. However, if a surface/lower tropospheric temperature inversion is present, the progression of the RGB signal can actually be reversed, such that it appears less pink with increasing dust. Such atmospheric profiles are often encountered over the North African region through the night and into early morning.

[44] Attempting to match specific SEVIRI window channel observations to simulations using colocated point measurements is challenging because of the discrepancy in scale between the data sets and the large variability seen over relatively short distances, particularly in surface skin temperature and surface emissivity. Nevertheless, we are able to achieve reasonable consistency between simulations and SEVIRI observations during the early morning over the SAMUM ground station at Tinfou. Later in the day the point observations of skin temperature seem inconsistent with the satellite observations, being biased low by ~5–10 K. Nevertheless, the fact that the RGB imagery fails to turn pink over Tinfou at both times, despite significant dust optical depth estimates from ground-based Sun photometer and visibility measurements, is well captured by the simulations.

[45] One aspect that we have not attempted to investigate in this study is the potential impact of cloud on the RGB imagery. If a dust layer is overlain by optically thick cloud then it will be masked in the dust RGB imagery. Conversely, if the overlying cloud is semitransparent, for example, cirrus anvil outflow, then it may confound the signal seen because of its conflicting spectral signature in the window region [e.g., *Ackerman et al.*, 1990]. With this in mind it is useful to also be aware of the other RGB composites that can be derived from alternative SEVIRI channel combinations (LR08), which are designed to highlight specific cloud microphysical properties.

[46] In spite of the limitations we have identified, the SEVIRI RGB dust imagery product has already proved to be an extremely useful monitoring tool for the climate and weather forecasting community. We hope that the work outlined here provides helpful guidelines of when the imagery can be confidently employed, and when it should be used with more caution. One particular step that could be relatively easily implemented is to superpose contours of CWV on the imagery to assist with its interpretation. In future work we will assess how dust climatologies produced by objective approaches such as that suggested by Ashpole and Washington (submitted manuscript) are affected by the points we raise here, and investigate whether additional rendering tools can be developed to circumvent some of these issues.

[47] **Acknowledgments.** H.B. was funded by NERC grant NE/D009197/1. P.K. acknowledges funding from ERC grant 257543, "Desert Storms." We would like to thank Albert Ansmann for providing the ground-based broadband IR measurements made at Ouarzazate and Oliver Schulz for providing IMPETUS station data.

References

Ackerman, S., W. Smith, J. Spinhirne, and H. Revercomb (1990), The 27–28 October 1986 FIRE IFO cirrus case study: Spectral properties of cirrus clouds in the 8–12 μm window, *Mon. Weather Rev.*, *118*, 2377–2388, doi:10.1175/1520-0493(1990)118<2377:TOFICC>2.0.CO;2.

Anderson, G., et al. (2000), MODTRAN4: Radiative transfer modeling for remote sensing, in *Algorithms for Multispectral, Hyperspectral, and Ultraspectral Imagery VI*, edited by S. S. Chen and M. R. Descour, *Proc. SPIE Int. Soc. Opt. Eng.*, *4049*, 176–183, doi:10.1117/12.410338.

Bierwirth, E., et al. (2009), Spectral surface albedo over Morocco and its impact on radiative forcing of Saharan dust, *Tellus, Ser. B*, *61*, 252–269.

Bou Karam, D., C. Flamant, J. Cuesta, J. Pelon, and E. Williams (2010), Dust emission and transport associated with a Saharan depression: February 2007 case, *J. Geophys. Res.*, *115*, D00H27, doi:10.1029/2009JD012390.

Brindley, H., and R. Allan (2003), Simulations of the effects of interannual and decadal variability on the clear-sky outgoing long-wave radiation spectrum, *Q. J. R. Meteorol. Soc.*, *129*, 426–446, doi:10.1256/qj.02.216.

Brindley, H., and J. Russell (2006), Improving GERB scene identification using SEVIRI: Infrared dust detection strategy, *Remote Sens. Environ.*, *104*, 426–446, doi:10.1016/j.rse.2006.05.019.

DeSouza-Machado, S., L. Strow, S. Hannon, and H. Motteler (2006), Infrared dust spectral signatures from AIRS, *Geophys. Res. Lett.*, *33*, L03801, doi:10.1029/2005GL024364.

European Organisation for the Exploitation of Meteorological Satellites (2006), MSG SEVIRI spectral response characterization, *Rep. EUM/MSG/TEN/06/0010*, Darmstadt, Germany. [Available at http://www.eumetsat.int/Home/Main/Satellites/MeteosatSecondGeneration/Instruments/index.htm.]

Fouquart, Y., B. Bonnel, G. Brogniez, J. Buriez, L. Smith, and J.-J. Morcrette (1987), Observations of Saharan aerosols: Results of ECLATS field experiment, part II, Broadband radiative characteristics of aerosols and vertical flux divergence, *J. Clim. Appl. Meteorol.*, *26*, 38–52, doi:10.1175/1520-0450(1987)026<0038:OOSARO>2.0.CO;2.

Hansell, R., Jr., J. Reid, S. Tsay, T. Roush, and O. Kalashnikov (2011), A sensitivity study on the effects of particle chemistry, asphericity and size on the mass extinction efficiency of mineral dust in the Earth's atmosphere: From the near to thermal IR, *Atmos. Chem. Phys.*, *11*, 1527–1547, doi:10.5194/acp-11-1527-2011.

Haywood, J., P. Francis, S. Osborne, M. Glew, N. Loeb, E. Highwood, D. Tanré, G. Myhre, P. Formenti, and E. Hirst (2003), Radiative properties and direct radiative effect of Saharan dust measured by the C-130 aircraft during SHADE: 1. Solar spectrum, *J. Geophys. Res.*, *108*(D18), 8577, doi:10.1029/2002JD002687.

Haywood, J., R. Allan, I. Culverwell, A. Slingo, S. Milton, J. Edwards, and N. Clerbaux (2005), Can desert dust explain the outgoing longwave radiation anomaly over the Sahara during July 2003?, *J. Geophys. Res.*, *110*, D05105, doi:10.1029/2004JD005232.

Heintzenberg, J. (2009), The SAMUM-1 experiment over southern Morocco: Overview and introduction, *Tellus, Ser. B*, *61*, 2–11.

Hess, M., P. Koepke, and I. Schult (1998), Optical properties of aerosols and clouds: The software package OPAC, *Bull. Am. Meteorol. Soc.*, *79*, 831–844, doi:10.1175/1520-0477(1998)079<0831:OPOAAC>2.0.CO;2.

Highwood, E., J. Haywood, M. Silverstone, S. Newman, and J. Taylor (2003), Radiative properties and direct effect of Saharan dust measured by the C-130 aircraft during Saharan Dust Experiment (SHADE): 2. Terrestrial spectrum, *J. Geophys. Res.*, *108*(D18), 8578, doi:10.1029/2002JD002552.

Horvath, H. (1971), On the applicability of the Koschmieder visibility formula, *Atmos. Environ.*, *5*, 177–184, doi:10.1016/0004-6981(71)90081-3.

Hsu, N., S. Tsay, M. King, and J. Herman (2004), Aerosol properties over bright-reflecting source regions, *IEEE Trans. Geosci. Remote Sens.*, *42*, 557–569, doi:10.1109/TGRS.2004.824067.

Johnson, B., M. Brooks, D. Walters, S. Woodward, S. Christopher, and K. Schepanski (2011), Assessment of the Met Office dust forecast model using observations from the GERBILS campaign, *Q. J. R. Meteorol. Soc.*, *137*, 1131–1148, doi:10.1002/qj.736.

Kandler, K., et al. (2009), Size distribution, mass concentration, chemical and mineralogical composition and derived optical parameters of the boundary layer aerosol at Tinfou, Morocco, during SAMUM 2006, *Tellus, Ser. B*, *61*, 32–50.

Klüser, L., D. Martynenko, and T. Holzer-Popp (2011), Thermal infrared remote sensing of mineral dust over land and ocean: A spectral SVD based retrieval approach for IASI, *Atmos. Meas. Tech.*, *4*, 757–773, doi:10.5194/amt-4-757-2011.

Knippertz, P. (2008), Dust emissions in the West African heat trough—The role of the diurnal cycle and of extratropical disturbances, *Meteorol. Z.*, *17*, 553–563, doi:10.1127/0941-2948/2008/0315.

Knippertz, P., and M. C. Todd (2010), The central west Saharan dust hot spot and its relation to African easterly waves and extratropical disturbances, *J. Geophys. Res.*, *115*, D12117, doi:10.1029/2009JD012819.

Knippertz, P., C. Deutscher, K. Kandler, T. Müller, O. Schulz, and L. Schütz (2007), Dust mobilization due to density currents in the Atlas region: Observations from the SAMUM 2006 field campaign, *J. Geophys. Res.*, *112*, D21109, doi:10.1029/2007JD008774.

Knippertz, P., et al. (2009), Dust mobilisation and transport in the northern Sahara during SAMUM 2006—A meteorological overview, *Tellus, Ser. B*, *61*, 12–31.

Koepke, P., M. Hess, I. Schult, and E. Shettle (1997), Global Aerosol Data Set, *MPI Rep. 243*, 44 pp., Max-Planck-Inst. für Meteorol., Hamburg, Germany.

Lensky, I., and D. Rosenfeld (2008), Clouds-aerosols-precipitation satellite analysis tool (CAPSAT), *Atmos. Chem. Phys.*, *8*, 6739–6753, doi:10.5194/acp-8-6739-2008.

Li, J., P. Zhang, T. Schmit, J. Schmetz, and W. Menzel (2007), Technical note: Quantitative monitoring of a Saharan dust event with SEVIRI on Meteosat-8, *Int. J. Remote Sens.*, *28*, 2181–2186, doi:10.1080/014311606:00975337.

Liu, D., A. Wang, Z. Liu, D. Winker, and C. Trepte (2008), A height resolved global view of dust aerosols from the first year of CALIPSO lidar measurements, *J. Geophys. Res.*, *113*, D16214, doi:10.1029/2007JD009776.

Marsham, J., D. Parker, C. Grams, C. Taylor, and J. Haywood (2008), Uplift of Saharan dust south of the intertropical discontinuity, *J. Geophys. Res.*, *113*, D21102, doi:10.1029/2008JD009844.

Martinez, M., J. Ruiz, and E. Cuevas (2009), Use of SEVIRI images and derived products in a WMO sand and dust storm warning system, *IOP Conf. Ser. Earth Environ. Sci.*, *7*, 012004, doi:10.1088/1755-1307/7/1/012004.

McConnell, C., E. Highwood, H. Coe, P. Formenti, B. Anderson, S. Osborne, S. Nava, K. Desboeufs, G. Chen, and M. Harrison (2008), Seasonal variations of the physical and optical characteristics of Saharan dust: Results from the Dust Outflow and Deposition to the Ocean (DODO) experiment, *J. Geophys. Res.*, *113*, D14S05, doi:10.1029/2007JD009606.

Miller, M., and A. Slingo (2007), The ARM Mobile Facility and its first international deployment: Measuring radiative flux divergence in West Africa, *Bull. Am. Meteorol. Soc.*, *88*, 1229–1244, doi:10.1175/BAMS-88-8-1229.

Müller, D., et al. (2010), Mineral dust observed with AERONET Sun photometer, Raman lidar, and in situ instruments during SAMUM 2006: Shape-independent particle properties, *J. Geophys. Res.*, *115*, D07202, doi:10.1029/2009JD012520.

Peres, L., and C. DaCamara (2005), Emissivity maps to retrieve land-surface temperature from MSG/SEVIRI, *IEEE Trans. Geosci. Remote Sens.*, *43*, 1834–1844, doi:10.1109/TGRS.2005.851172.

Schepanski, K., I. Tegen, B. Laurent, B. Heinold, and A. Macke (2007), A new Saharan dust source activation frequency map derived from MSG-SEVIRI IR-channels, *Geophys. Res. Lett.*, *34*, L18803, doi:10.1029/2007GL030168.

Schepanski, K., I. Tegen, M. Todd, B. Heinold, G. Boenisch, B. Laurent, and A. Macke (2009), Meteorological processes forcing Saharan dust emission inferred from MSG-SEVIRI observations of subdaily dust source activation and numerical models, *J. Geophys. Res.*, *114*, D10201, doi:10.1029/2008JD010325.

Schulz, O., M. Finck, and H. Goldbach (2010), Hydro-meteorological measurements in the Drâa catchment, in *Impacts of Global Change on the Hydrological Cycle in West and Northwest Africa*, edited by P. Speth, M. Christoph, and B. Diekrüger, pp. 122–131, Springer, Heidelberg, Germany.

Seemann, S., E. Borbas, R. Knuteson, G. Stephenson, and H.-L. Huang (2008), Development of a global land surface emissivity database for application to clear sky sounding retrievals from multi-spectral satellite radiance measurements, *J. Appl. Meteorol. Climatol.*, *47*, 108–123, doi:10.1175/2007JAMC1590.1.

Shettle, E., and R. Fenn (1979), Models for the aerosols of the lower atmosphere and the effects of humidity variations on their optical properties, *Rep. AFGL-TR-79–0214*, Air Force Geophys. Lab., Hanscom AFB, Mass.

Slingo, A., et al. (2008), Overview of observations from the RADAGAST experiment in Niamey, Niger: Meteorology and thermodynamic variables, *J. Geophys. Res.*, *113*, D00E01, doi:10.1029/2008JD009909.

Sokolik, I., and O. Toon (1999), Incorporation of mineralogical composition into models of the radiative properties of mineral aerosol from UV to IR wavelengths, *J. Geophys. Res.*, *104*, 9423–9444, doi:10.1029/1998JD200048.

Torres, O., A. Tanskanen, B. Veihelmann, C. Ahn, R. Braak, P. Bhartia, P. Veefkind, and P. Levelt (2007), Aerosols and surface UV products from ozone monitoring instrument observations: An overview, *J. Geophys. Res.*, *112*, D24S47, doi:10.1029/2007JD008809.

Turner, D. (2008), Ground-based infrared retrievals of optical depth, effective radius, and composition of airborne mineral dust above the Sahel, *J. Geophys. Res.*, *113*, D00E03, doi:10.1029/2008JD010054.

Vickery, K. (2010), Southern African dust sources as identified by multiple space borne sensors, MSc thesis, Dep. of Environ. and Geogr. Sci., Univ. of Cape Town, Cape Town, South Africa.

Volz, F. (1973), Infrared optical constants of ammonium sulphate, Sahara dust, volcanic pumice, and flyash, *Appl. Opt.*, *12*, 564–568, doi:10.1364/AO.12.000564.

World Climate Program (1986), A preliminary cloudless standard atmosphere for radiation computation, *Rep. WMO/TD 24*, World Meteorol. Org., Geneva, Switzerland.

I. Ashpole, School of Geography and the Environment, University of Oxford, Oxford OX1 3QY, UK. (ian.ashpole@sjc.ox.ac.uk)

H. Brindley, Space and Atmospheric Physics Group, Imperial College London, London SW7 2AZ, UK. (h.brindley@imperial.ac.uk)

P. Knippertz, School of Earth and Environment, University of Leeds, Leeds LS2 9JT, UK. (p.knippertz@leeds.ac.uk)

C. Ryder, Department of Meteorology, University of Reading, Reading RG6 6BB, UK. (c.l.ryder@reading.ac.uk)